

Slow Drag in 2D Granular Media

Junfei Geng and R. P. Behringer

Department of Physics and Center for Nonlinear and Complex Systems, Duke University,

Durham NC, 27708-0305, USA

(February 2, 2008)

Abstract

We study the drag force experienced by an object slowly moving at constant velocity through a 2D granular material consisting of bidisperse disks. The drag force is dominated by force chain structures in the bulk of the system, thus showing strong fluctuations. We consider the effect of three important control parameters for the system: the packing fraction, the drag velocity and the size of the tracer particle. We find that the mean drag force increases as a power-law (exponent of 1.5) in the reduced packing fraction, $(\gamma - \gamma_c)/\gamma_c$, as γ passes through a critical packing fraction, γ_c . By comparison, the mean drag grows slowly (basically logarithmic) with the drag velocity, showing a weak rate-dependence. We also find that the mean drag force depends non-linearly on the diameter, a of the tracer particle when a is comparable to the surrounding particles' size. However, the system nevertheless exhibits strong statistical invariance in the sense that many physical quantities collapse onto a single curve under appropriate scaling: force distributions $P(f)$ collapse with appropriate scaling by the mean force, the power spectra $P(\omega)$ collapse when scaled by the drag velocity, and the avalanche size and duration distributions collapse when scaled by the mean avalanche size and duration. We also show that the system can be understood using simple failure models, which repro-

duce many experimental observations. These observations include: a power law variation of the spectrum with frequency characterized by an exponent $\alpha = -2$, exponential distributions for both the avalanche size and duration, and an exponential fall-off at large forces for the force distributions. These experimental data and simulations indicate that fluctuations in the drag force seem to be associated with the force chain formation and breaking in the system. Moreover, our simulations suggest that the logarithmic increase of the mean drag force with rate can be accounted for if slow relaxation of the force chain networks is included.

PACS numbers: 46.10.+z, 47.20.-k

I. INTRODUCTION

Granular materials are of great interest for their rich phenomenology and import applications [1]. When subject to external stresses, a dense granular system forms inhomogeneous force chain networks where only a fraction of the grains carry most of the force [2]. The spatial scale of these force chains can extend over many grain diameters, and the chain lengths may be comparable to the system size. The separation between microscopic and macroscopic scales poses a theoretical challenge if one attempts to describe a granular system using continuum approach. Recently, experimental works by several research groups [3,4,7–9,11] suggest the importance of strong stress fluctuations in granular systems. The fluctuations, as characterized by the standard deviation or *rms* of the stress, can often be somewhere from 1 to several times of the mean stress. However, questions involving the dynamics, nature, and length/time scales associated with these fluctuations are still poorly understood. An improved understanding of these questions could provide insight into describing a number of practical applications and such phenomena as earthquakes and avalanches. Another motivation concerns exploring jamming [19,39] in granular materials. Specifically, jammed states in granular systems may be reached when the density (packing fraction) of the system is high enough.

In this regard, slow drag experiments, the subject of this paper, provide a useful way to understand the nature of stress fluctuations and slow dynamics in granular materials. We have used a similar experimental approach to probe the thermodynamic temperature in granular systems, as reported elsewhere [15].

In molecular fluids, the drag force on a particle arises from viscous interactions, i.e. from collisional interactions of the particle and surrounding molecules that involve momentum transfer. This drag force is linearly proportional to the object's velocity through the fluid when the velocity is not very large.

In dense granular media, the origin of the drag force differs in several respects. First, frictional interactions exist between a drag particle and surrounding grains. Second, but re-

lated, is the existence of force chains. These relatively long-range inhomogeneous structures can provide an elastic (rigid in the limit of infinitely stiff particles) resistance to a moving particle.

In Fig. 1c, we show such force chain structures obtained using photoelastic techniques [8,22]. These force chains are typically inhomogeneous and anisotropic in nature, and constantly form and break when an object moves through the granular media, leading to strong fluctuations in the drag force. In the experiments presented here, we consider the drag force experienced by a tracer particle moving through a 2D granular material consisting of bidisperse disks. In our experiment, the size of the tracer particle is comparable to the surrounding grains, which allows us to explore fluctuations at the grain scale. The experimental results presented here are described well by simple failure models.

A number of experimental and theoretical results provide important background to the present studies. Experiments that are relevant here include the “carbon paper” studies of Mueth et al. [4], who measured the static forces of a material (e.g. glass beads) at the boundary of a container, and showed that the distribution of forces, f , is exponential for large f . Sheared granular systems, both in 2D [8,9] and 3D [7], show strong force/stress fluctuations. In addition, the 2D experiments by Howell et al. [8] showed a well defined strengthening/softening transition as the packing fraction of the system passed a critical packing fraction γ_c . The mean stress in such a system varies as a power-law in the reduced packing fraction,

$$r = \frac{\gamma - \gamma_c}{\gamma_c}, \quad (1)$$

with an exponent between 2 and 4, depending on the particle type. Later experiments on similar 2D systems by Hartley et al. [9] showed that the mean stress increased logarithmically with the shearing rate, which may be related to collective slow relaxation of the force chain network. 3D experiments by Miller et al. [7] identified rate-independent power spectra, $P(\omega)$, for the stress time series which fell off as $P \sim \omega^{-2}$ at high spectral frequency ω . Experiments on 3D drag by Albert et al. [12,11,13] relate most closely to the present experiments. These

studies yielded the drag force experienced by a rod as it was dragged through granular materials such as glass beads. Depending on the rod insertion depth and the size ratio between the rod and the grain, three types of drag force time series were observed: a periodic regime where the signal resembles an ideal sawtooth pattern, a random regime, and a stepped regime with sawtooth-like steps. These authors focused their work on the periodic and stepped regimes, characterized by stick-slip fluctuations due to successive formation and collapse of jammed states. A particularly interesting finding of these studies was that the mean drag force on the rod was independent of the drag velocity.

Several theoretical works [14,16] have provided a context for understanding the stress distributions and stress fluctuations in granular materials. The q-model of Coppersmith et al. [14] predicts a force distribution for static systems $P(F) \propto F^{N-1} \exp(-F/F_0)$, where N is the system dimension. This model only considers the vertical force transmitted through a regularly packed lattice. Vertical forces on a grain in one layer are balanced by transmitting fractions, q and $(1-q)$, to the two supporting grains in the next layer (assuming a 2D system), where q is a random number uniformly distributed in $0 \leq q \leq 1$. We note for exponential force distributions, that the mean is of the order of the width of the distribution. Other lattice models [29] and calculations by Radjai using contact dynamics [30] also predict exponential force distributions for large forces.

Recently, Kahng et al. [16] have used a stochastic failure model to understand the 3D drag experiments of Albert et al. [12,11,13]. These authors used simple springs with random thresholds to model the jamming and reorganization of grains. Among other results, the model reproduces the experimentally observed periodic sawtooth fluctuations in the drag force. We will use this simple failure model, with modifications, later in this paper to understand the experiments described here.

The organization of the remainder of this paper is as follows. In Section II, we describe the experimental setup and procedures. In Section III, we report experimental results. In Section IV, we describe models and simulations. Finally, we draw conclusions in Section V.

II. EXPERIMENTAL SETUP AND PROCEDURES

The experiments were carried out in an apparatus which is, in spirit, similar to the one in Ref. [12], except that the one used here is two-dimensional in character, whereas the one used by Albert et al. was three-dimensional. We show a cross-sectional view of the apparatus in Fig. 1a. The bottom plate was driven by the center shaft, both of which are supported by ball bearings mounted on a stable metal table (not shown). A stepper motor ran at a low frequency to drive the bottom plate. The top plate did not rotate and had no contact with the rotating bottom plate or the particles. The granular medium consisted of a single layer of bi-disperse disks with diameters 0.744 and 0.876 cm, where the thickness of both types of disk was 0.660 cm. Fig. 1b shows an actual image from the experiment where the two types of disks can be identified. The disks were placed on the bottom plate and confined between two concentric ring structures. The inner ring radius was 10.5 cm and the outer ring radius was 25.4 cm. When the bottom plate was rotating, the disks moved with it as a rigid body, due to friction. This frictional force with the substrate was relatively weak compared to the forces between particles associated with force chains. The centrifugal force experienced by the disks was negligible due to the slow rotation speed. Note that this apparatus is not to be confused with a Couette shearing apparatus where either the inner wheel or the outer wheel is moving. In this apparatus, both inner and outer boundaries remained fixed and the driving was provided by the moving bottom plate.

A digital force gauge (Model DPS-110 from Imada Inc., resolution 0.1 g), shown in the inset of the Fig. 1a, was mounted on one side of the top plate. The force sensor was connected with a tracer particle through a hole, located in the center of the inner and outer ring. The reading on the force gauge, which yielded the instantaneous tangential force, was recorded as a time series by a computer through its serial communication port, as in Fig. 2. When the granular medium moved, force chains form in the bulk of the system, as show in Fig. 1c using photoelastic techniques [8,22]. The pins on the left side of the top plate stirred the particles.

There are three important parameters that we explored in the system, i.e, the rotation rate ω , the system packing fraction γ (or density), and the tracer particle size a . We varied the rotation rate ω over two orders of magnitude, from $\omega = 6.33 \times 10^{-6}$ to $8.67 \times 10^{-4} Hz$ (corresponding to $v = 7.14 \times 10^{-6}$ to $9.78 \times 10^{-4} m/s$), the packing fraction γ from 0.561 to 0.761 (these values are global packing fractions since the system is not completely uniform), and the tracer particle diameters over the set of diameters $a = 0.744, 0.876, 1.250, 1.610$ and 1.930 cm.

III. EXPERIMENTAL RESULTS

In this section, we report the experimental results. We first consider the effect of rotation rate, and we then turn to the effect of changes in the packing fraction.

A. Changing the Medium Rotation Rate

An initial series of experiments was carried out at a fixed packing fraction $\gamma = 0.754$, which is above the critical packing fraction γ_c , discussed in more detail in the next section. Here, we varied the rotation rate over $\omega = 6.33 \times 10^{-6} \leq \omega \leq 8.67 \times 10^{-4} Hz$ (corresponding to $7.14 \times 10^{-6} \leq v \leq 9.78 \times 10^{-4} m/s$). (The velocity of the tracer is $v = \omega r$, where $r = 17.95$ cm is the radial location of the tracer.) In Fig. 2, we show three sets of force time series, obtained with a tracer size $a = 0.876$ cm, and rotation rates that spanned the full range of ω 's, namely (a). $\omega = 6.3 \times 10^{-6} Hz$, (b). $\omega = 5.0 \times 10^{-4} Hz$, and (c). $\omega = 8.7 \times 10^{-4} Hz$. As one would expect, the force time series in Fig. 2 show strong fluctuations. Interestingly, an enlarged view of a small section of Fig. 2c, seems qualitatively similar to the slower run in Fig. 2a, which suggests possible scaling behavior. We will return to this point below.

1. Mean Drag Force and Force Distributions

In Fig. 3a, we show the mean drag force, $\langle F \rangle$, as a function of rotation rate, ω , for tracer particles of five different diameters ($a = 0.744, 0.876, 1.25, 1.61$ and 1.93 cm.). For each of these tracer sizes, the mean drag force increased only slightly (by a factor less than 2) for a variation by more than two decades in ω . To emphasize this slow increase, we plot the same data on log-lin scales in Fig. 3b. The data can be fitted by a straight line, indicating a logarithmic variation of $\langle F \rangle$ with ω . This is consistent with the results by Hartley et al. [9] who found that the total stress in a system of similar particles undergoing slow shearing also increases logarithmically with the shearing rate.

We emphasize that this slow increase in the mean force differs significantly from the drag force in a fluid, where the mean force increases linearly with the drag velocity when the velocity is not too large. This is also in contrast to rate-independent stresses in Mohr-Coulomb friction models [5,6] for dense granular systems. It is consistent with several rate-dependent friction models [31].

In Fig. 4, we show the standard deviation of the drag force, $StdDev(F)$, as a function of the rotation rate, where $StdDev(F) = \sqrt{\frac{1}{N} \sum_{i=1}^N (F_i - \langle F \rangle)^2}$. N is the number of measurements in the force time series and F_i is the i th measurement. We note that the standard deviation is of the same order of magnitude as its corresponding mean, and that it also increases roughly logarithmically with the rate.

The slow increase of the mean drag force with rate appears to differ from experimental observations in some previous studies, including those by Wiegard and by Albert et al. [32,12]. In particular, Wiegard [32] measured the drag force experienced by vertical rods dipped into a rotating bed of fine dry sand. In this case, the drag force had a weak dependence on the velocity: first decreasing then increasing with increasing velocity. In the experiments by Albert et al. [12], the mean drag force on a cylindrical rod was found to be independent of the drag velocity.

In the case of Wiegard's experiments, the explanation for the difference is relatively

straightforward. The velocity range used in Wieghard's experiments is very different from both that used in our and Albert et al.'s measurements. Wieghard investigated velocities ranging from about 0.2 m/s to 2 m/s; the minimum of the drag force appeared between 0.5 m/s and 1 m/s depending on the rod insertion depth. Wieghard explained the variation of drag with speed in the following way. The normal pressure and the frictional forces along the slip surface provided resistance. At lower speed, the inertial force of the sand flowing around the body was small and negligible. When the velocity increased, there was a reduction in drag because, presumably, more contacts were slipping and kinetic friction is smaller than static friction. At larger speeds, friction became less dependent on the velocity; however, when the velocity was increased, an additional inertial term led to an increase in the drag force.

The velocities used in the Albert et al. experiments and in the current experiments (of the order of 1 mm/s) are more comparable and are much slower than that of Wieghard. To a first order approximation, the present data is consistent with Albert's data, i.e. they both show that the mean force is roughly independent of the velocity. However, we do see a slow, logarithmic increase in the mean force that differs from the observation of Albert et al.

The explanation for this difference is not known, but it is interesting to speculate on the cause. Of course, there is the obvious difference in dimensionality. However, another difference between the two experiments is that the present particles were softer (a lower Young's modulus) than those used by Albert et al. In the present experiments, the particles deformed elastically, whereas in the experiments of Albert et al. an external spring was deformed. The real issues include differences in the elastic time scales vs. characteristic times for frictional events (e.g. creation and destruction of force chains.) and the amount of elastic deformation of particles. In this regard, we note the work by Campbell [10]. Recent experiments by Hartley et al. [9] using the same type of particles as those of the present experiments showed a qualitatively similar relation between the mean force and the rate, albeit in a Couette system. These experiments also showed that under static shear stresses, there was a logarithmically slow relaxation of the force network. Later in this work, we will

use a modified failure model inspired by this observation to reproduce the slow increase in the mean drag force.

In Fig. 5, we show drag force distributions for different rotation rates. The left panel of Fig. 5 gives force distributions for a tracer particle of diameter $a = 0.744$ cm, and the right panel gives data for $a = 1.93$ cm. From Fig. 5a, c, we note that, irrespective of the particle size, the force distributions broaden and shift towards larger forces as the rotation velocity increases. Interestingly, these force distributions collapse into a single curve when scaled by the corresponding mean force, as shown in Fig. 5b, d. Thus, the mean force is one of the key control parameters for this system. These data indicate a roughly exponential fall-off for large forces, as seen in Fig. 5b, d, which shows the scaled distributions on semi-log scales. As the tracer size increases, one noticeable change in the force distributions is that the probability of very small force becomes smaller. An intuitive explanation is that a larger tracer particle is more likely to be in contact with some strong force chains at any time, thus reducing the probability of a very small force. This argument must be modified for tracers that are much larger than the background particles. As the tracer particle diameter becomes very large, there are multiple contacts, some of which involve strong force chains, and we expect that the distribution for $F / \langle F \rangle$ will no longer depend on the tracer diameter.

2. Power Spectra and Correlations

The power spectra, $P(\omega)$, resulting from such force time series provide a useful quantitative measure of the relevant time scales for force fluctuations. (Note that the mean force has been removed in calculating the spectra.) In Fig. 6a, we show $P(\omega)$ vs. the frequency, ω , on log-log scales. At high frequency, the spectra fall off as $P(\omega) \propto 1/\omega^\alpha$, with $\alpha \simeq 2$. At low frequency, the spectra vary more weakly, and are almost independent of the frequency. The $1/\omega^2$ behavior at high frequency can be explained by assuming a series of random jumps occurring on time scales at least as fast as a crossover time $\sim 1/\omega^*$. This time corresponds roughly to the time for the tracer particle to travel a few disk diameters. We will come

back to this time scale below in more detail. The power spectrum at low frequency is presumably explained by the fact that there are no strong correlations at very long time scales in the force time series. A $1/\omega^2$ behavior occurs in many other contexts, e.g. for frictional fluctuations [17] and stick-slip motions [18].

These spectra also show interesting rate invariance. In Fig. 6b, we rescale the power spectra data of Fig. 6a by dividing the ω -axis by the corresponding rotation rate, ω_0 , and multiplying P by ω_0 . This corresponds to rescaling time by $1/\omega_0$, or alternatively by replacing time by angular displacement. Fig. 6b shows an excellent collapse of all the data for the scaled power vs. the scaled frequency, and implies rate invariance in the fluctuating component of the stresses. Such rate-invariance in stress fluctuations has also been observed by Miller et al. [7] and Albert et al. [13]. An argument for this rate invariance is provided in Ref. [33] which suggests that the system spends much of its time in states close to static equilibrium, so that ω_0 sets the time scale to move between states.

We can better understand the role of ω^* by calculating the correlations resulting from these force time series. In Fig. 7a, we show correlation functions, $C(t)$, for time series at different rotation rates (Note that $C(\Delta t) = \langle F(t)F(t + \Delta t) \rangle$, where the brackets denote an average of time, and $C(\Delta t)$ is simplified as $C(t)$ when no confusion is caused). These correlation functions generally drop quickly (exponentially) to zero over a time scale of t_c , and then fluctuate around zero, indicating that the signals are uncorrelated beyond that time. If we rescale the data of Fig. 7a by multiplying the t -axis by the corresponding velocities, all correlation functions collapse to a single curve, as shown in Fig. 7b. The collapsed curve defines a characteristic length scale, Δx_c , which is comparable to one disk diameter. Intuitively, this can be explained by the fact that force chains contacting the tracer particle tend to form and then fail when the tracer particle moves by a few grain diameters, in agreement with the characteristic length scale revealed in Fig. 7b.

We note here that the correlation data and the power spectra data are a Fourier Transform pair according to the Wiener-Khinchin Theorem [35]. Thus, the $1/\omega^2$ power spectrum at high frequency can also be derived from the correlation data at small time scales. Using

the fact (inset of Fig. 7b) that the correlation functions decay exponentially at early time as: $C(t) = A_0 \cdot \exp(-t/t_c)$, the corresponding power spectrum can be obtained by performing a Fourier transform:

$$\begin{aligned} P(\omega) &= \int_{-\infty}^{\infty} C(t) \exp(-i\omega t) dt \\ &= \frac{2t_c}{1 + (\omega t_c)^2} \\ &\approx \omega^{-2}, \text{ if } \omega \gg 1/t_c. \end{aligned}$$

Thus, for large frequency ($\omega \gg 1/t_c$), we expect the power spectrum will decay as $1/\omega^2$.

3. Avalanches and the Force Chain Force Constant.

If we define an avalanche event to be a monotonic decrease in the force time series, we can investigate the stress release process in the system more quantitatively (similar results are found for the stress build-up process). This approach is similar in spirit to the approach of self-organized criticality (SOC) [27], and it is interesting to ask whether any sign of SOC is present in this system.

We denote the size of an avalanche to be the magnitude of the drop of the force and the duration to be the time it takes for an avalanche event to take place, as illustrated in Fig. 8. With such definitions, we can calculate the probability distributions for both avalanche sizes and avalanche durations. We show such distributions (properly rescaled) in Fig. 9 for force time series obtained at different velocities. It is possible to collapse all the distributions for avalanche size by dividing the horizontal coordinate for each set of data by the corresponding mean avalanche size and (and therefore necessarily multiplying the vertical coordinate by the mean avalanche size). The avalanche duration distributions are similarly rescaled by the corresponding mean avalanche duration of each data set. In Fig. 9, we show both data sets on log-lin scales, which emphasizes the roughly exponential nature of the distributions. The flat tails at larger values of the horizontal coordinates may be due to insufficient statistics.

These data suggest that there is a large probability of finding small avalanche events in the system, while the probability of finding a large avalanche event becomes exponentially small. Note that these distributions do not show any indication of power laws, as one would expect for a self-similar process and SOC.

It is interesting to ask how the mean avalanche size and duration change with ω . We show, in Fig. 10a, data for the mean avalanche size, $\overline{\Delta F}$, and duration, $\overline{\Delta t}$, as functions of the rotation rate. The mean avalanche size increases with ω and the mean avalanche duration decreases with ω . Both the mean size and the mean duration vary as power laws with ω . Particularly interesting is the fact that the ratio of the mean avalanche size to duration, Fig. 10b, also varies essentially linearly as a power of ω . The linear relationship between $\overline{\Delta F}/\overline{\Delta t}$ and ω (or the medium velocity v) suggests that there is an effective 'spring constant' for the force chains, that can be defined as $\overline{\Delta F}/(v\overline{\Delta t})$. We develop this point further in the next few paragraphs.

An obvious question is whether a large avalanche event (in terms of its size) is in general associated with a longer duration, or perhaps vice-versa. This question is addressed in Fig. 11 by calculating the 2D probability distributions for avalanches sizes and durations. These distributions are given in Fig. 11a-c for different drag velocities, using a greyscale representation. We see that these distributions are always distributed around certain directions with positive slopes, which suggests that, in general, a larger avalanche event lasts longer. We also note that the slope of the distribution orientation increases with increasing drag velocity. Based on the scalings of Fig. 9, if we rescale the vertical and horizontal axis in Fig. 11 by the mean avalanche size and mean avalanche duration, respectively, we expect that the resulting distributions for different velocities would be peaked around the same orientation. Indeed we have tested that this is the case.

Since the 2D distributions for avalanche size and duration, Fig. 11, tend to be oriented around a certain direction, it is useful to consider an alternative approach to characterize these events. Namely, we define the avalanche rate to be the ratio of the avalanche size

and the corresponding duration, i.e., $Rate = \frac{Size}{Duration} = \frac{\Delta F}{\Delta t}$. We show the distributions of rates for different medium velocities in Fig. 12a. From this figure, we see first that each distribution is peaked, which is consistent with our claim that events have a most probable direction in Fig. 11, albeit with some spreading around that direction. Secondly, this figure shows that when the rotation rate increases, the position of the peak shifts to the right.

We extract the peak positions and plot them as a function of the medium velocity, Fig. 12b. This figure shows that the peak position increases roughly linearly with the medium velocity. If we denote the slope of a least-squares linear fit to this data as k_{eff} , then:

$$k_{eff} = \frac{\Delta F}{\Delta t} \frac{1}{v} = \frac{\Delta F}{\Delta x}. \quad (2)$$

Thus, k_{eff} resembles the force constant of a simple spring. Indeed, Fig. 1c shows that the resisting forces are mainly carried through chain-like structures, and one might imagine that each of these force chains acts like a spring. The collective force constant of these force chains is then rather well defined, as suggested by the quantity, k_{eff} , extracted from Fig. 12b. One has to keep in mind that since Fig. 12b is obtained only for peak positions, the actual effective force constant at a given instant can vary around the k_{eff} extracted here. A similar observation has been made in Ref. [16] by Kahng et al. concerning their 3D drag experiment (see Fig. 2 in Ref. [11]). However, the force constant revealed in those experiments reflects only the force constant of the external spring. That is, since it is much softer than the effective spring constant of the grains, the force registered on the force sensor is mainly due to the compression of the external spring. By contrast, in our experiments, the effective force constant gives a measurement of actual strength of the force chains in the granular system. Specifically, the force constant of the external spring in our apparatus is much stronger than that associated with the particles.

The above analysis supports the idea that force chains may be modeled by springs as proposed in the model by Kahng et al. [16]. In Section IV below, we modify their model to explain features of the data for the current experiments.

In the remainder of this section, we explore several other features of the experimental

results.

B. Changing the Packing Fraction

In this section, we describe experimental data and analysis associated with changing the packing fractions in the system. For this set of experiments, we fixed the rotation rate at $\omega_0 = 5.0 \times 10^{-4} Hz$ and the tracer size at $a = 1.25$ cm.

1. Mean Drag Force and Force Distributions

When we change the packing fraction, γ , we observe a softening/strengthening transition similar to the one reported in Ref. [8]. Specifically, when γ is below a critical value, γ_c , the system is so loosely packed that it cannot sustain force chains. In the regime $\gamma < \gamma_c$, when the grains make contact with the tracer particle, they are almost immediately pushed into open space, and no long-range force chains form. On the contrary, when the packing fraction is above the critical value $\gamma \geq \gamma_c$, there are always some force chains in the bulk of the system, such as those shown in Fig. 1c. In Fig. 13, we show three sets of force time series data obtained at different γ 's. For the data of $\gamma = 0.561$, which is below $\gamma_c = 0.645$, the forces are close to zero, with a small amount of activity corresponding to those events when the tracer particle makes contact with grains. When $\gamma = 0.653$, which is slightly above γ_c , we already see more activity, and the average force signal increases above the base line. When γ is increased further, say to $\gamma = 0.754$, the force signal become much more active and the scale of fluctuations is significantly larger.

Fig. 14a shows the mean drag force as a function of the global packing fraction γ . We identify two different regimes in this figure. For smaller γ 's, the mean force can be fitted by a linear function of γ : $F = a\gamma + b$, where a and b are constants, while for larger γ 's, the mean force can be fitted by a power-law, which parallels the results of Howell et al. [33]: $F = F_c + d(\gamma - \gamma_c)^\beta$, where d and β are constants. We define γ_c as the crossover value from the linear to the non-linear regime. In Fig. 14b, we show the mean force as a function of

reduced packing fraction, $r = \frac{\gamma - \gamma_c}{\gamma_c}$, for $\gamma \geq \gamma_c$ on log-log scales to emphasize the power-law character in the nonlinear regime. In that regime, the exponent of the power law is $\beta = 1.53$.

In Fig. 15a, we show drag force distributions for different packing fractions. As the packing fraction is increased, the distributions widen and the means becomes larger, consistent with the data of Fig. 14. Again, if we rescale the force distributions by the corresponding mean force, we obtain an approximate collapse of all curves. Thus, the mean force is also the appropriate scaling factor for the amplitude of the drag force fluctuations.

Thus far, we have considered the mean properties and distributions of the drag forces for different rotation rates and packing fractions. We now combine these results and examine how the control parameters, ω and γ , affect the drag force.

Fig. 16 shows the combined drag force distributions for various rotation rates and packing fractions. The solid symbols are data for different ω 's, and the open symbols are data for different γ 's. All the distributions are rescaled by their corresponding mean drag forces. Again, we see all rescaled curves have nearly the same form. This statistical invariance in the force distributions is striking, since these data are obtained over a wide range of rotation rates (more than two decades) and packing fractions. This again confirms the key scaling role of the mean force. We note too that these distributions decay roughly exponentially for large forces, in the spirit of the q-model [14].

For a given tracer particle, changing the rotation rate or changing γ both affect the mean drag force, although the former is only a weak effect. In Fig. 17a, we combine the data for mean drag forces from Fig. 3 and 14 in a single plot, where the top axis is the rotation rate, ω , and the bottom axis is the reduced packing fraction $r = (\gamma - \gamma_c)/\gamma_c$. When γ is fixed, the mean force (solid circles) increases slowly with ω , where this slow increase is adequately described as a logarithm. When ω is fixed, the mean force (solid squares) increases rapidly with γ , and this increase is described by a power-law. If we assume that \bar{F} can be written in a product form as $\bar{F} = f_1(a)f_2(\omega)f_3(r)$, for our given tracer particle size, we find that a good description of the data is given by:

$$\bar{F} = \frac{1}{14.51}(22.802 + 2.588 \log \omega)(2.502 + 174.91r^{1.529}). \quad (3)$$

Fig. 17b shows the mean drag force \bar{F} in a 3D perspective plot. From this figure, we see that an increase of the rotation rate, ω , leads to an increase of the mean drag force, qualitatively resembling what occurs due to an increase in the packing fraction, γ , but on a much weaker scale. Similar effects on the stress due to changes in the shear rate and packing fraction were also observed in a 2D granular Couette systems [9].

We also examine how the diameter of the tracer particle, a , affects the mean drag force. In Fig. 18, we show the mean drag force as a function of the tracer diameter for different rotation rates at a given packing fraction $\gamma = 0.754$. From these data, we see that the increase in the mean force with tracer particle size is faster than linear.

It is interesting to contrast these results with what one would expect for a particle, typically much larger than a molecule, that is moving through a viscous fluid. According to Stokes's law [36], the drag force, is proportional to the diameter of the tracer particle, the coefficient of viscosity of the fluid, and the relative velocity of the fluid and the tracer.

It is also interesting to compare our results to the experiments by Albert et al. [13] on drag through a granular material. As noted, these authors observed rate independent forces. They also found a linear dependence of the drag force on the diameter of the drag rod. However, it is perhaps not surprising that in the present experiments the diameter dependence of the drag force is nonlinear, since the tracer particle size is comparable to the size of surrounding grains (the maximum size ratio is 2.6), unlike the situation in the experiments of Albert et al.

2. Rescaling of Power Spectra and Avalanches

In Fig. 19a, we show power spectra of force time series for different packing fractions. In this case, variations of the power spectra with γ are qualitatively similar to those due to changes in the rotation rate shown in Fig. 6a, although the magnitude of the changes with γ is much greater. It is interesting to rescale these spectra to see if they will collapse onto

a common curve. In this regard, we note from Parseval's Theorem [35], that the integral of the power spectral density over frequency is equal to the mean square amplitude of the signal, i.e.,

$$\frac{1}{2\pi} \int_{-\infty}^{\infty} P(\omega) d\omega = \frac{1}{2\pi} \int_{-\infty}^{\infty} |F(\omega)|^2 d\omega = \int_{-\infty}^{\infty} |f(t)|^2 dt, \quad (4)$$

where $F(\omega)$ and $f(t)$ are a Fourier pair. Hence, the integral of the power spectrum, which is proportional to the mean square amplitude of force signals, $\langle f^2 \rangle = \int_{-\infty}^{\infty} |f(t)|^2 dt$, can be used as an appropriate scale factor for the spectra in Fig. 19a. Indeed, when these spectra are normalized by the corresponding $\langle f^2 \rangle$, we obtained a good collapse of data, as shown in Fig. 19b. Additionally, we show the scaling factor, $\langle f^2 \rangle$, vs. the reduced packing fraction, r , in Fig. 20. These data can also be fitted to a power law, and the exponent is almost twice as large as the exponent associated with the power-law for the mean force, Fig. 14.

Before turning to the model, we note that the avalanche data calculated from force time series for different packing fractions are similar to those for different rotation rates. We have tested that distributions for both avalanche size and duration decay exponentially, and can be rescaled by the respective mean avalanche size and duration to obtain good collapse of the data.

IV. MODEL AND SIMULATIONS

In this section, we turn to a stochastic failure model, based on one originally proposed by Kahng et al. [16] to understand the experimental data of Albert et al. [12,11]. We modify this model appropriately to account for several features that are unique to the present 2D granular system. Specifically, we make two modifications to the original model:

i) First, we allow the band of thresholds to be wide enough so as to generate random force patterns, and we use exponentially distributed thresholds to produce more realistic force distributions;

ii) Second, we introduce a time-dependent threshold to explain the slow (logarithmic) increase of the mean drag force with the rate.

We also note that since the particles are only one layer deep in the 2D experiments, we do not need any depth dependence. In the reminder of this section, we first briefly introduce the basic model. We then make modifications to the model and perform simulations to compare with the present experimental data.

A. The Original Spring Model

The original model was constructed to simulate the drag force experienced by a vertical cylinder inserted to a given depth in a granular bed [16]. In this model, the grains move with constant speed v in the x-direction, and the tracer particle is simply represented by a block, as shown in Fig. 21a. The tracer particle interacts with grains that are assumed to be supported by force chains. The particle-tracer interactions are modeled as linear springs with a force constant k_0 , where there are n such springs. (The assumption of a single spring constant is in part justified for the present data by the analysis of an effective force chain force constant, k_{eff} , in the experimental data as in Fig. 12.) Necessarily, the spring constant, k_{eff} , refers to the collective mean response, instead of a force constant for an individual force chain. As time advances, each spring is compressed by an amount Δx , which is determined by the velocity v and by Δt , the time interval over which compression has occurred, i.e.

$$f = f_0 + k_0 \Delta x = f_0 + k_0 v \Delta t, \quad (5)$$

where, f_0 is a small initial force proportional to the local pressure in the system. This is illustrated in Fig. 21b. At $t = 0$, a spring makes contact with the tracer particle, corresponding to the formation of a force chain. The spring is then compressed as time advances. If the spring (force chain) is too compressed, e.g., the force f exceeds a threshold, g , the spring fails, and the force on the spring is relaxed to f_0 . In addition, the threshold g is updated to a new value chose at random from an appropriate distribution. In the original model, g was

uniformly distributed over an interval $[g_0, g_1]$. Over time, the process of spring compression (force chain formation) and failure continues. At any given time, the drag force is the sum of the forces from all n springs.

The original model [16] also assumes that the effective force chain springs are much stronger than the external spring associated with the machine that is pushing the tracer. In such a case, the drag force, which is typified by stick-slip dynamics, is a function of the strength of the external spring. Khang et al. focused on the stick-slip regime, since this corresponded to what was observed in the 3D drag experiments by Albert et al.

However, in the present experiments, the effective spring constant of the drive is significantly larger than that of the particles. Consequently, we do not observe stick-slip behavior, but rather random force fluctuations. We must take into account this different feature of our experiments, and we now turn to appropriate modifications of the model.

B. Modification I: Wide Threshold Bands and Exponentially Distributed Thresholds

We begin by considering the effect of the width of the threshold band $[g_0, g_1]$. As one would expect, this width qualitatively affects the drag force patterns. When the threshold band is narrow, as in Fig. 13a, for $[g_0, g_1] = [0.49, 0.51]$, the force time series exhibits a regular sawtooth pattern. This is because all the springs fail almost at the same time, resulting in a regular pattern of buildup and release. When the threshold band is wider, the force pattern becomes more random (e.g., $[g_0, g_1] = [0.1, 0.9]$). This more closely resembles what occurs in the the present experiments.

However, if the threshold g is uniformly distributed between $[g_0, g_1]$, the resulting force distributions are symmetric with respect to the mean drag force, as shown in Fig. 13b for a 10 spring system. The symmetry of this distribution differs from those of the experiment, and simply reflects the symmetry of the failure distribution. The data of avalanche size distribution in Fig. 9 suggest that the probability of finding a large event becomes exponentially small. Thus, it is reasonable to assume that the distribution of g 's is like-

wise exponential. We expect that most of the time, the force chains break at small forces, and only in rare events, do the force chains survive to reach a large threshold. Using this assumption, we obtain a force time series such as that shown in Fig. 13c. We show the resulting force distributions (for 10 springs) in (d). In contrast to Fig. 13b, these new force distributions obtained with exponentially distributed thresholds are significantly closer in appearance to the experimental data, as in Fig. 15.

Note that the mean force in the model is found by summing over n independent variables, x_i , where x_i is the compression of spring i . The mean value of any one of these is then $\bar{x}_i = (1/2)\bar{g}$, where \bar{g} is the mean determined from the distribution of g 's. As n grows, we expect that the distribution of total force F will approach a Gaussian with a mean value $n\bar{g}$ and a width $\sqrt{n}\sigma$, where σ^2 is the variance of g . Indeed, the statistical properties of the model follow from the fact that the force is a sum over n uncorrelated random variables where the maximum of each variable is drawn from the appropriate distribution of g 's.

Apart from the force distributions, for other aspects of the simulated data (power spectra, distributions of avalanche size/duration, and force chain force constants), uniformly distributed thresholds do not lead to significantly different results than thresholds that are exponentially distributed, as long as the threshold band is wide enough. Below, we will focus on the simulated data derived from exponentially distributed thresholds.

In Fig. 23, we show power spectra and their rescaled form for different velocities calculated from the model. These data are in remarkable qualitative agreement with the experimental data shown in Fig. 6.

In Fig. 24, we show in (a) the distributions of avalanche sizes derived from the model simulations and in (b) the rescaled distributions of avalanche durations derived from the model simulations. Both distributions of avalanche size and duration are roughly exponential for large arguments, as are the experimental data, Fig. 9. Note, however, that the size distributions in this figure are not rescaled while those in Fig. 9a are.

Similarly, in Fig. 25, we show avalanche rate distributions at different velocities in (a) and the derived effective force chain force constant in (b). This figure compares well with

the experimental data shown in Fig. 12. The effective force chain force constant from the simulation data is $k_{eff} = 30.7$, which is of the same order of magnitude as nk_0 , where $n = 10$ (the number of springs) and $k_0 = 1$ (the individual force constant of a spring).

C. Modification II: Decaying Thresholds

The model so far has been able to reproduce a number of experimental observations. However, if we calculate the mean drag force, $\langle F \rangle$, as a function of the medium velocity, v , we find that $\langle F \rangle$ is independent of v , as shown in Fig. 26. Fig. 26a shows force distributions for several different velocities, and they all fall on the same curve, with almost the same mean and variance. Fig. 26b is a direct plot of mean drag force as a function of velocity, which shows a rate-independent result. This differs from the experimental finding that the mean drag force increases logarithmically with the velocity.

The fact that the model is rate-independent is not surprising. The instantaneous force state is found by summing over the n springs. The state of each spring does not depend on the velocity of the block, but only on the displacement of the block since it was last reset to f_o . In such a displacement-controlled system, there can be no velocity dependence.

One possible way to account for the rate-dependence is to recognize that there is failure of some contacts due to creep, and we explore that possibility here. In this regard, we note recent work by Hartley et al. (Fig. 2 in [9]) involving similar particles to those used here. These authors reported logarithmically slow relaxation of the force chain network in their 2D granular Couette system. Specifically, in these experiments, 2D photoelastic grains were sheared steadily so as to establish a strong force chain network. The shearing was abruptly stopped and the particle-scale forces in a section of the Couette annulus were monitored thereafter. The force chains relaxed (became weaker) over many hours, with the total stress in the system decaying logarithmically slowly, presumably due to the collective rearrangements of the grains and failure under creep at contacts that were near to failure. Such failures became progressively more difficult over time because, presumably, the con-

tacts near failure became less numerous, and also perhaps due to geometric constraints on successive rearrangements.

To make a connection with the model, we note that one interpretation of the Hartley et al. experiments was that the force chains become logarithmically weaker over time, which means that the threshold of each spring should decrease with time. This is illustrated in Fig. 27. For two processes with different velocities ($v_1 > v_2$), if the originally chosen thresholds for a spring are g in each case, by the time a spring reaches its failure point, this threshold has become smaller. Since $v_2 < v_1$, by the time failure actually occurs, the threshold for the slow process (v_2) is smaller than that of the fast process (v_1). The longer one waits, the smaller the threshold. Hence, we assume the threshold, g , is time-dependent and decreases logarithmically with a time constant t_0 :

$$g(t) = 1 - \frac{\log t}{\log t_0}, \quad (6)$$

where, t_0 is a large value (about 10^5 times the time step) that sets the slow relaxation time scale/amplitude.

With such a decaying threshold, $g(t)$, we recalculate the drag force distributions and mean drag force for the model. In Fig. 28, we show the drag force distributions for different velocities in (a), and their rescaled form in (b). Comparison of Fig. 28 with the experimental data in Fig. 5 shows very good agreement. Fig. 29a shows the mean drag force from the simulation, which now has a slow increase with velocity. Fig. 29b shows the same data on a log-lin plot. These results can be fitted by a straight line, indicating a logarithmically slow increase now built into the model. This figure compares well with the experimental data in Fig. 3. Additionally, this modification to the model does not qualitatively change the features reported in previous sections.

In summary, the key point of the model is its assumption that the force chains are modeled as “springs” with failure thresholds chosen from a distribution. Thus, the fluctuations and mean properties of the drag force are closely associated with the force chain formation and failure. This understanding is useful in particular because it underscores the impor-

tant role of the force chains in granular systems. The elastic nature of the model is also interesting, given the current debate over how forces are transmitted in granular systems [40].

Another interesting observation from the experiments is the seeming contradiction between the rate-dependence in the mean properties (e.g., mean drag force vs. velocity, mean avalanche size vs. velocity, etc.) and the rate-independence of the fluctuations (e.g., rate-independent power spectra, collapse of the avalanche size distributions, etc.) in the data. However, this may be understood by noting that the mean behavior (or the DC part of the signal) is rate-dependent, while fluctuations (or the AC part of the signal) are rate-independent. This is also consistent with the failure model we have discussed; i.e., once the level of the mean behavior is set, the fluctuating components are subsequently set by the mean behavior.

V. CONCLUSIONS

To conclude, through experiments and simple failure models, we have characterized the drag force experienced by an object moving slowly through a 2D granular material consisting of bidisperse disks. The drag force is dominated by force chain structures in the bulk of the system. The formation and failure of the force chains leads to strong fluctuations.

We have considered the effect of three control parameters: the medium velocity, the packing fraction and the tracer particle size. Experimentally, we find that the mean drag force grows slowly (logarithmically) with the drag velocity, increases rapidly (power-law) with the packing fraction above a critical value, and varies nonlinearly with the size of the tracer particle. The system exhibits strong statistical invariance in the sense that many physical quantities collapse into a single curve under appropriate scaling: force distributions $P(f)$ collapse when scaled by the mean force, power spectra $P(\omega)$ collapse when scaled by the drag velocity, and avalanche size and duration distributions collapse when scaled by the mean values of these quantities.

We also show that the system can be understood using a simple failure model, which reproduces many experimental observations including: a power law with exponent $\alpha = -2$ for the high-frequency portion of the power spectrum, exponential distributions for the avalanche size and duration, and an exponential fall-off at large forces for the force distributions. The logarithmic increase of the mean force with the drag velocity can also be accounted for if slow relaxation of the material is included.

A number of questions remain. One of these is the nonlinear dependence of the drag force on the particle diameter. Heuristically, one might expect that the drag force would grow linearly in proportion to the number of force chains contacting the tracer, and that this would lead to a linear variation of the drag force with diameter. In this regard, the fact that the tracers used here were only somewhat larger than the grains is likely to be important. Obviously, the presence of weak rate dependence in the mean force is of interest, and its origin is still not clear. The relative elasticity of the particles (vs. the driving machinery) may be important in this regard, and future investigations with harder particles would be of interest. The frictional character of the drag force in the dense regime is clear in these experiments. It would be of interest to see what occurs as the packing fraction is reduced below γ_c . In the present experiments, the particles experience friction with the base, so that it is not possible to investigate the gas-like regime.

ACKNOWLEDGMENTS

We appreciate helpful interactions with R. Hartley and J. Matthews. The work was supported by the US National Science Foundation under Grant DMR-0137119, DMS-0204677, DMS-0244492, and by NASA under Grant NAG3-2372.

REFERENCES

- [1] For a broad perspective see Focus Issue on Granular Materials, *Chaos* **9**, 509–696 (1999); *Physics of Dry Granular Media*, H. J. Herrmann, J.-P. Hovi, and S. Luding, eds. NATO ASI Series, Kluwer, 1997; *Powders and Grains 97*, R. P. Behringer and J. T. Jenkins, eds. Balkema, 1997; H. M. Jaeger, S. R. Nagel, and R. P. Behringer, Rev. Mod. Phys. **68**, 1259 (1996); P.-G. de Gennes, Rev. Mod. Phys. **71**, 374 (1999).
- [2] P. Dantu, Géotechnique, **18**, 50 (1968); A. Drescher and G. De Josselin De Jong, J. Mech. Phys. Solids, **20**, 337 (1972); T. Travers et al. J. Phys. A. **19**, L1033 (1986).
- [3] G. W. Baxter and R. P. Behringer, Eur. J. Mech. B **10**, 181 (1991); C. H. Liu, and S. R. Nagel, Phys. Rev. Lett. **68**, 2301 (1992); G. W. Baxter, R. Leone and R. P. Behringer, Europhys. Lett. **21**, 569 (1993); A. Ngadi and J. Rajchenbach, Phys. Rev. Lett. **80**, 273 (1998);
- [4] D. M. Mueth, H. M. Jaeger, and S. R. Nagel, Phys. Rev. E **57**, 3164 (1998).
- [5] R. M. Nedderman, *Statics and Kinematics of Granular Materials*, Cambridge Univ. Press, Cambridge, (1992).
- [6] D. M. Wood, *Soil Behaviour and Critical State Soil Mechanics* (Cambridge University, Cambridge, England, (1990).
- [7] B. Miller, C. O'Hern and R.P. Behringer, Phys. Rev. Lett. **77**, 3110 (1996).
- [8] Daniel Howell, R.P. Behringer and Christian Veje, Phys. Rev. Lett. **82**, 5241 (1999).
- [9] R. Hartley and R.P. Behringer, Nature **421**, 928. (2003)
- [10] C. S. Campbell, J. Fluid Mech. **465**, 261 (2002).
- [11] I. Albert, P. Tegzes, B. Kahng, R. Albert, J.G. Sample, M. Pfeifer, A.L. Barabasi, T. Vicsek and P. Schiffer, Phys. Rev. Lett. **84**, 5122 (2000).
- [12] R. Albert, M.A. Pfeifer, A.L. Barabasi and P. Schiffer, Phys. Rev. Lett. **82**, 205 (1999).

- [13] I. Albert, P. Tegzes, R. Albert, J.G. Sample, A.L. Barabasi, T. Vicsek, B. Kahng, and P. Schiffer, Phys. Rev. E **64**, 031307 (2001)
- [14] C.-h. Liu, S. R. Nagel, D. A. Schecter, S. N. Coppersmith, S. Majumdar, O. Narayan and T. A. Witten, Science **269**, 513 (1995); S. N. Coppersmith, C.-h. Liu, S. Majumdar, O. Narayan and T. A. Witten, Phys. Rev. E **53**, 4673 (1996).
- [15] J. Geng and R. P. Behringer, Diffusion, mobility, and temperature in a stirred dense granular material, to be published. (2003).
- [16] B. Kahng, I. Albert, P. Schiffer and A.L. Barabasi, Phys. Rev. E. **64**, 051303 (2001).
- [17] A. L. Demirel and Steve Granick, B. Kahng, Phys. Rev. Lett. **77**, 4330 (1996).
- [18] M.G. Rozman, M. Urbakh and J. Klafter, Phys. Rev. Lett. **77**, 683 (1996).
- [19] A. L. Liu, and S. R. Nagel, Nonlinear Dynamics: Jamming is not just cool anymore. *Nature*. **396**, 21-22 (1998).
- [20] M. E. Cates, J. P. Wittmer, J. -P. Bouchaud and P. Claudin, Phys. Rev. Lett. **81**, 1841 (1998).
- [21] G. Reydellet and E. Clément, Phys. Rev. Lett. **86**, 3308 (2001).
- [22] J. Geng, D. Howell, E. Longhi, R.P. Behringer, G. Reydellet, L. Vanel, E. Clément and S. Luding, Phys. Rev. Lett. **87**, 0335506 (2001).
- [23] J-P. Bouchaud, P. Claudin and D. Levine, M. Otto, Euro. Phys. J. **E4**, 451 (2001).
- [24] J.E.S. Socolar, D.G. Schaeffer, P. Claudin, Euro. Phys. J. **E7**, 353 (2002).
- [25] D. A. Head, A. V. Tkachenko, T. A. Witten, Euro. Phys. J. **E6**, 99 (2001).
- [26] J. Duran, *Sands, Powders, and Grains: An Introduction to the Physics of Granular Materials* (Springer-Verlag, New York, 1999).
- [27] V. Frette, K. Christensen, J. Feder, T. Jossang and P. Meakin, Nature **379**, 49. (1996)

- [28] C.-h. Liu, S. R. Nagel, D. A. Schecter, S. N. Coppersmith, S. Majumdar, O. Narayan and T. A. Witten, *Science* **269**, 513 (1995), *Phys. Rev. E* **53**, 4673 (1996).
- [29] Christophe Eloy and Eric Clément, *J. Phys. I (France)* **7**, 1541 (1997); Mario Nicodemi, *Phys. Rev. Lett.* **80**, 1340 (1998); Joshua E. S. Socolar, *Phys. Rev. E* **57**, 3204 (1998).
- [30] F. Radjai, M. Jean, J.-J. Moreau, and S. Roux, *Phys. Rev. Lett.* **77**, 274 (1996).
- [31] See for example, A. Ruina, *J. Geophys. Res.* **88**, 10359 (1983); J. R. Rice and A. L. Ruina, *J. Appl Mech.* **50**, 343 (1983); E. Rabinowicz, *Proc. Phys. Soc. London* **71**, 668 (1958); F. Heslot, T. Bauberger, B. Perrin, B. Caroli and C. Caroli, *Phys. Rev. E* **49**, 4973 (1994).
- [32] K. Wieghard, *Annu. Rev. Fluid Mech.* **7**, 89 (1975).
- [33] R.P. Behringer, E. Clément, J. Geng, D. Howell, L. Kondic, G. Metcalfe, C. O'Hern, G. Reydellet, S. Tennakoon, L. Vanel, and C. Veje, *Lecture Notes in Physics*, vol. 567, pp. 351 -391 (2001).
- [34] R. B. Heywood, *Designing by Photoelasticity*. Chapman and Hall Ltd., London, (1952).
- [35] W. H. Press, B. P. Flannery, S. A. Teukolsky, W. T. Vetterling, *Numerical Recipes in C: The Art of Scientific Computing*, 2nd Edition, Cambridge University Press. (1992).
- [36] R.K. Pathria, *Statistical Mechanics*, 2nd ed., p.464, Butterworth-Heinemann, Oxford, 1996.
- [37] J.M. Ziman, *Models of Disorder*, Cambridge University Press, Cambridge. (1979).
- [38] J. Geng, E. Longhi, R.P. Behringer and D. Howell, *Phys. Rev. E* **64**, 060301(R), 2001.
- [39] M.E. Cates, J.P. Wittmer, J.-P. Bouchaud, and P. Claudin, *Phys. Rev. Lett.* **81**, 1841 (1998).
- [40] J. Geng, R.P. Behringer, G. Reydellet, and E. Clément, *Physica D* **182**, 274 (2003).

FIGURES

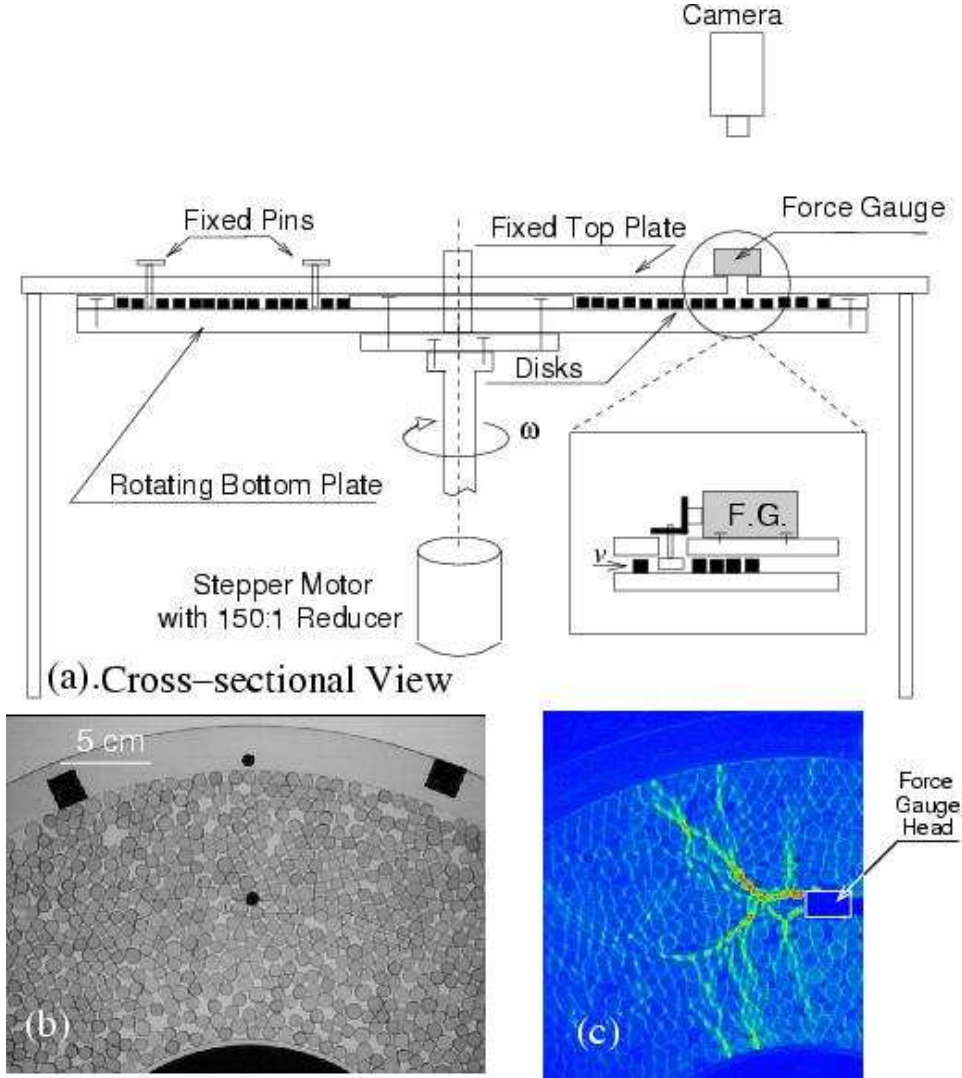


FIG. 1. (a). Schematic drawings of the apparatus: a cross-sectional view, where the plane of the section is through a diameter of the apparatus, which has circular symmetry in the horizontal plane. The bottom plate, together with particles, rotate as a rigid body at a slow velocity. The inset shows how a digital force gauge (F.G.) is mounted on the top plate and connected with the tracer particle through the force gauge hole. (b). An actual image taken from the experiments showing the 2D granular system composed of bidisperse disks. (c). A stress image, obtained using photoelasticity [8,22], showing force chain structures when the tracer particle is dragged through the medium.

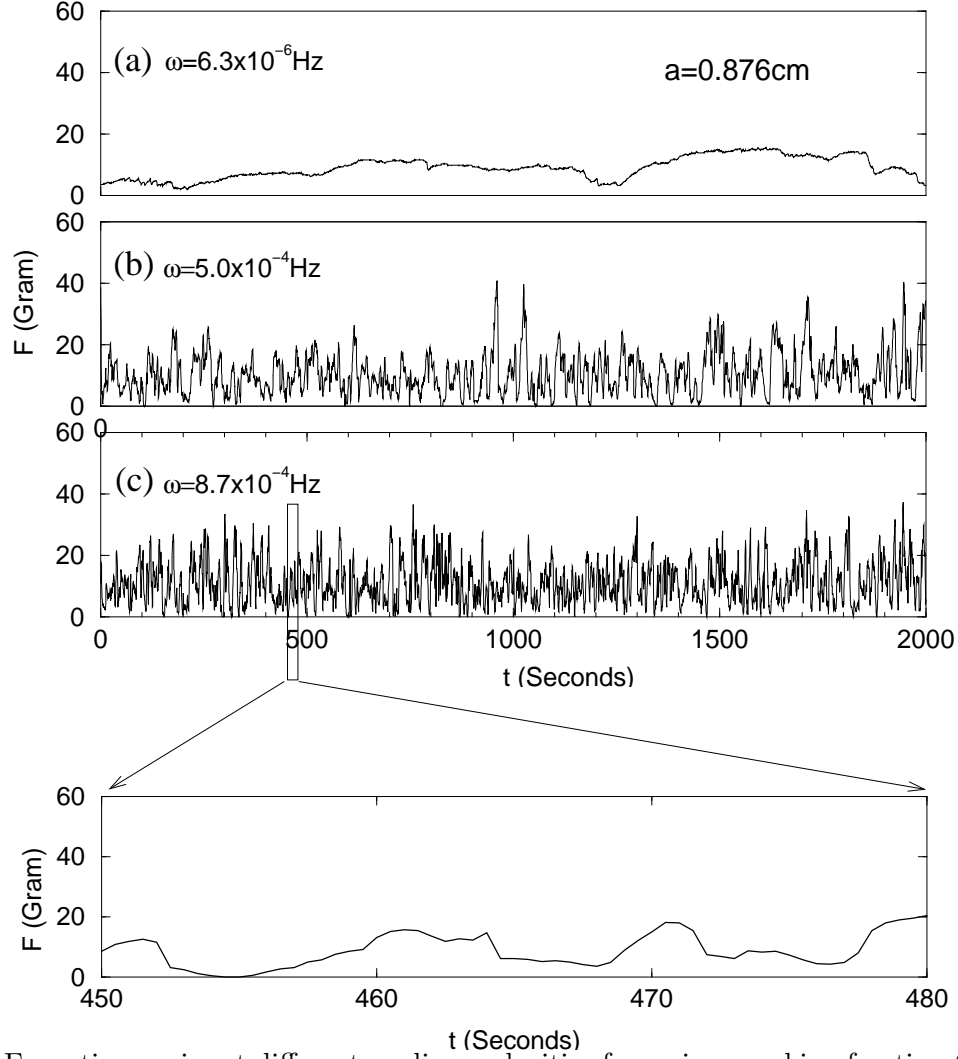


FIG. 2. Force time series at different medium velocities for a given packing fraction ($\gamma = 0.754$) and a given tracer size ($a = 0.876$ cm). The rotation rates are: (a). $\omega = 6.3 \times 10^{-6} \text{ Hz}$, (b). $\omega = 5.0 \times 10^{-4} \text{ Hz}$, and (c). $\omega = 8.7 \times 10^{-4} \text{ Hz}$. The velocity is obtained according to $v = \omega r$, where $r = 17.95$ cm. These force series show strong fluctuations. An enlarged view of a small segment of (c) also suggests self-similar structures in the system.

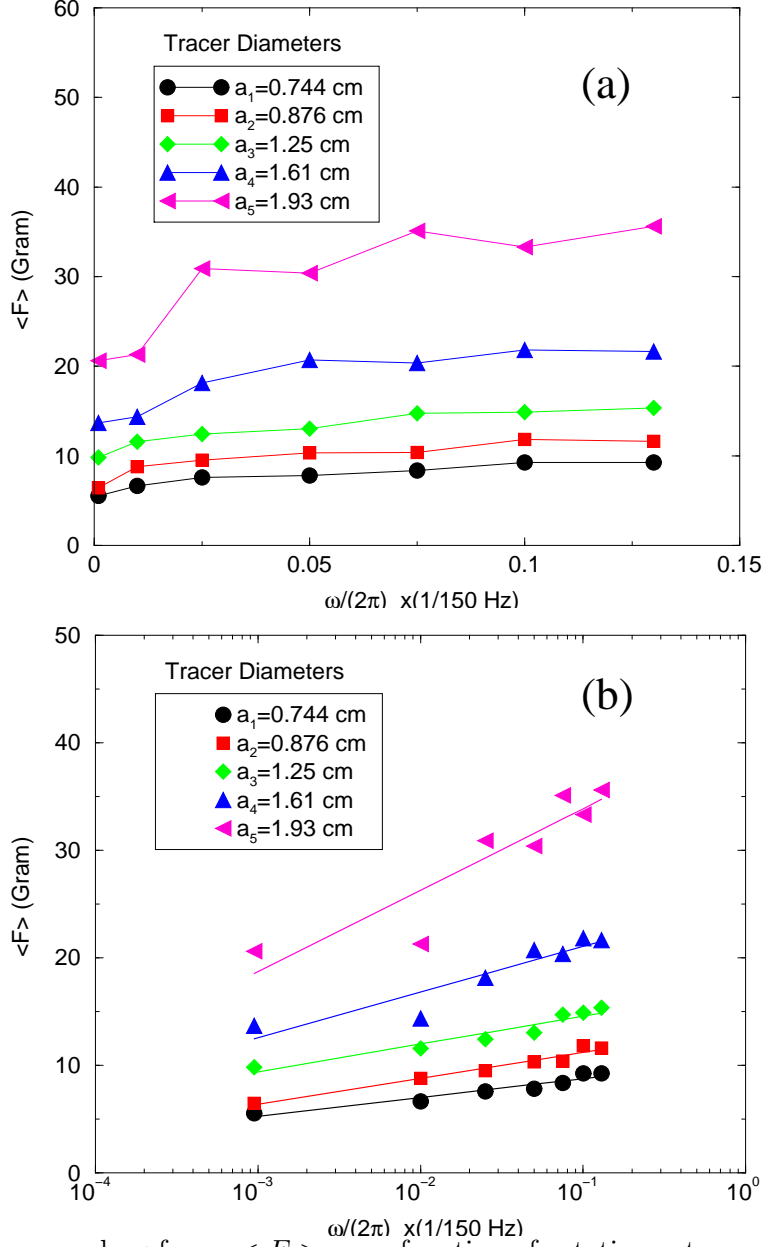


FIG. 3. (a) The mean drag force, $\langle F \rangle$, as a function of rotation rate, ω , for tracer particles with different sizes ($a = 0.744, 0.876, 1.25, 1.61$ and 1.93 cm). (b) Same data as (a), but on log-lin scales to emphasize that the mean force increases slowly (basically logarithmically) with the medium velocity. Throughout, we use a forces normalized by g , the acceleration of gravity.

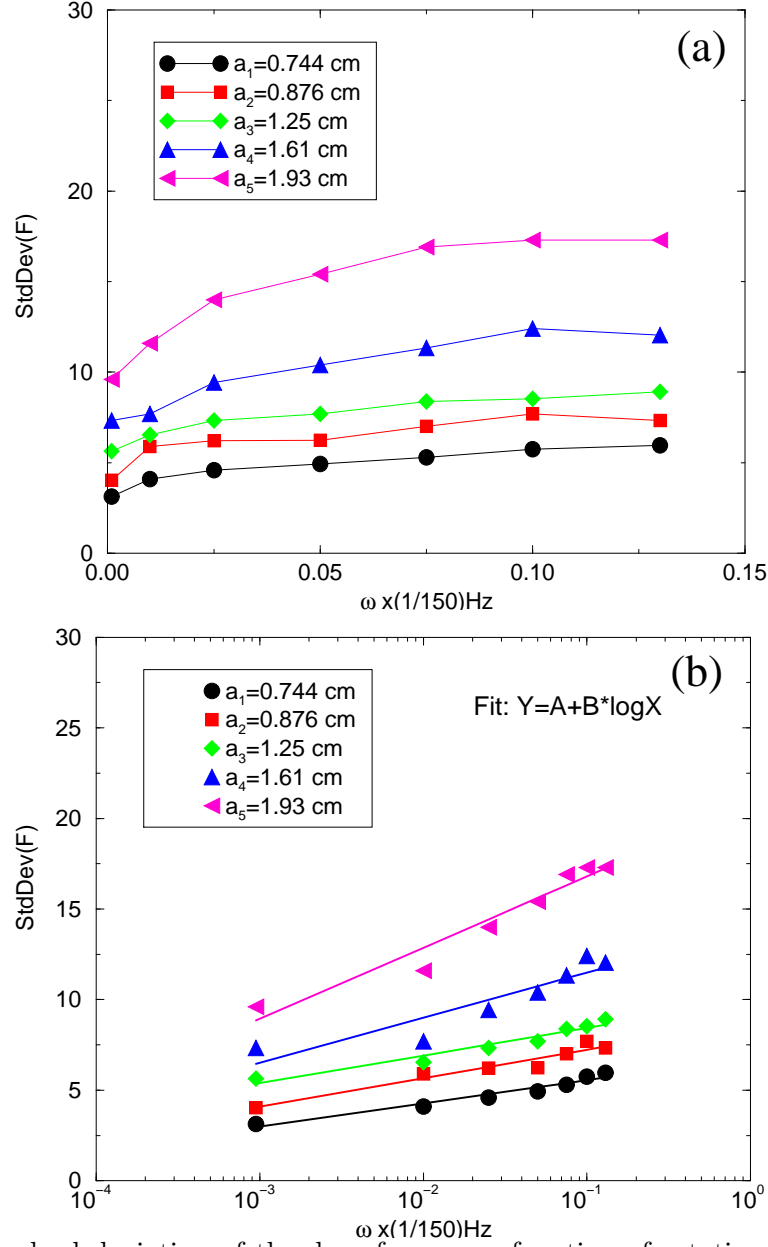
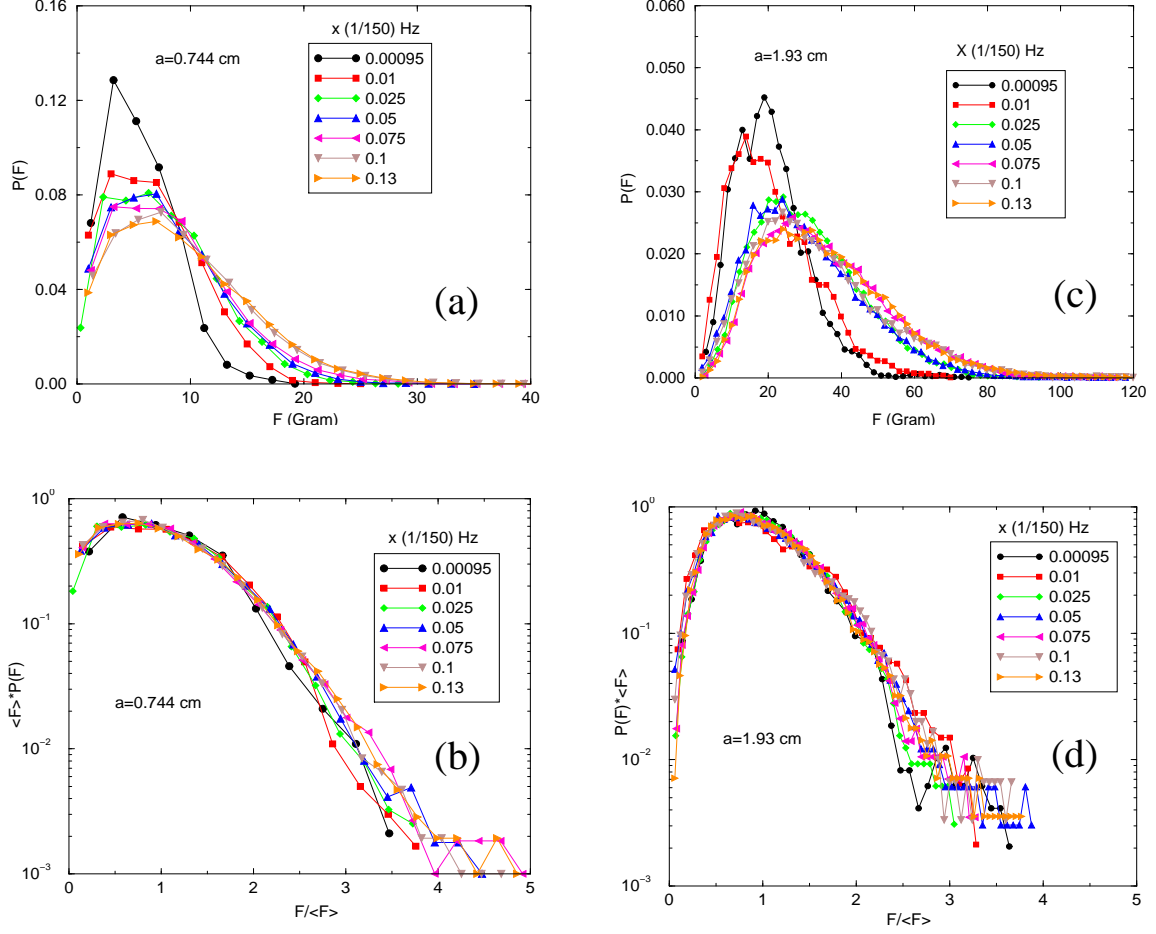


FIG. 4. (a) Standard deviation of the drag force as a function of rotation rate, ω , for tracer particles with different sizes ($a = 0.744, 0.876, 1.25, 1.61$ and 1.93 cm). (b) Same data as (a), but plotted on log-lin scales to emphasize that the standard deviation also increases logarithmically with the medium velocity.



Small Tracer

Large Tracer

FIG. 5. (a) Distributions of drag force at different rotation rates for a tracer particle of size $a = 0.744$ cm. (b) Same data as (a), but with the horizontal axis rescaled by the corresponding mean force, and the vertical axis multiplied by the mean force. The force distributions collapse to a single curve. Note that since the vertical axis in (b) is plotted on a logarithmic scale, the fall-off of the distribution at larger forces is roughly exponential. (c) and (d) are similar to (a) and (b), but for a larger tracer size $a = 1.93$ cm.

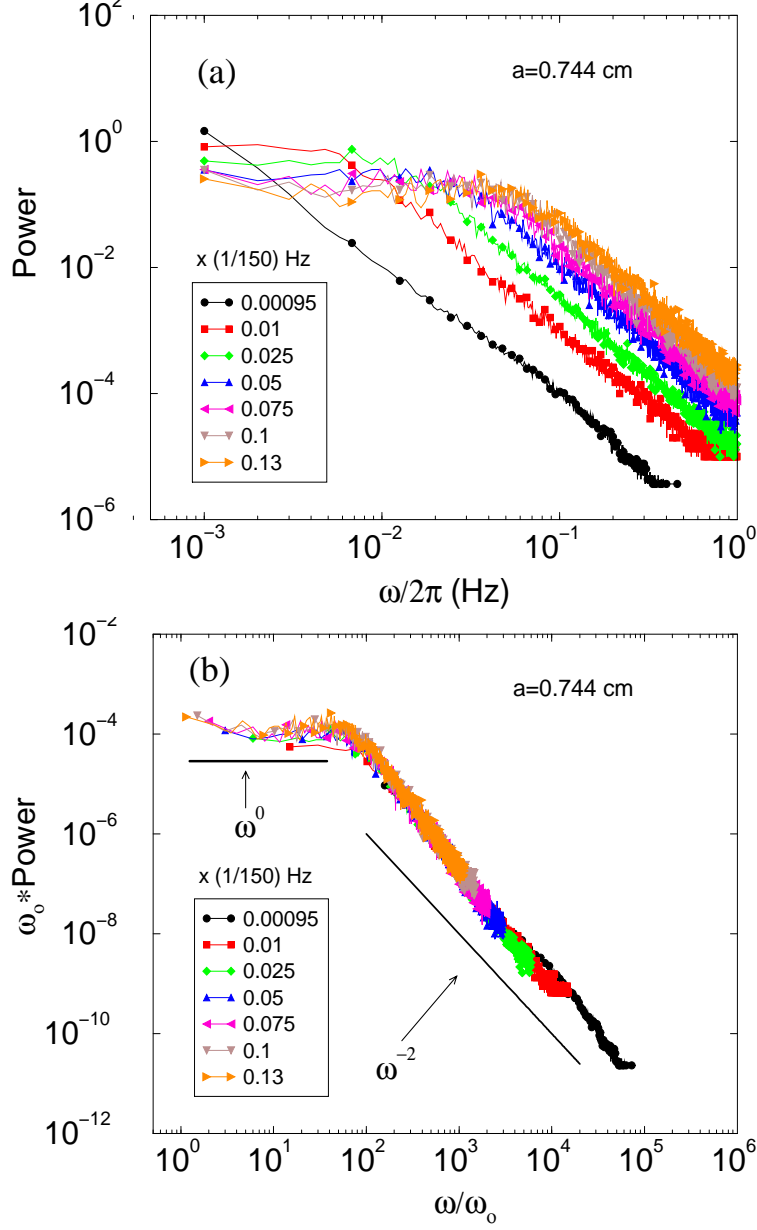


FIG. 6. (a) Power spectra, $P(\omega)$, from force time series at different rotation rates. (b) The scaled power, $\omega_o P(\omega)$ is plotted against the scaled frequency, ω/ω_o , where ω_o is the rotation rate. The data collapse nicely, demonstrating rate independence. At large spectral frequency ω , the power spectra vary as ω^{-2} , and at small frequency, the power spectra are flat, suggesting that there is no correlation at time scales larger than some constant factor of the inverse rotation rate.

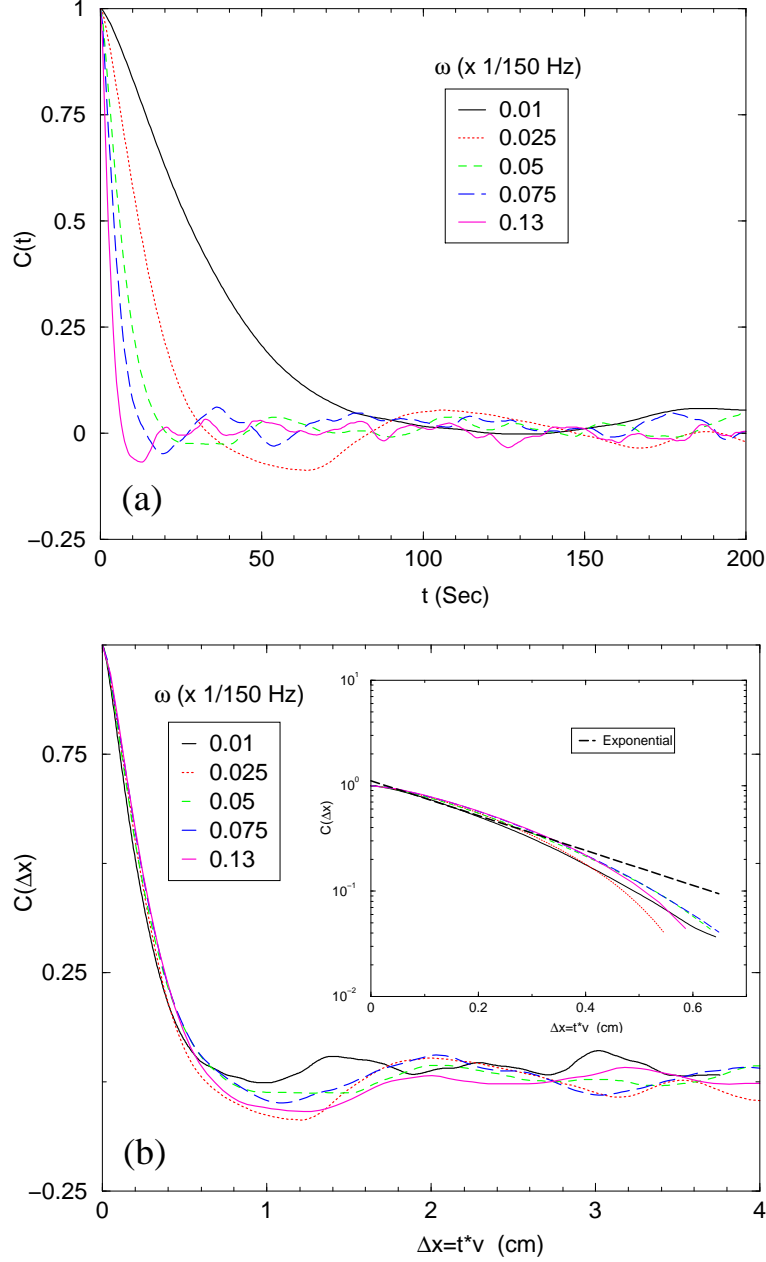


FIG. 7. (a) Correlation functions, $C(t)$, of the force time series at different rotation rates. We note that correlation functions at all rotation rates first drop quickly (exponentially) over a time scale of t_c , then fluctuate around zero. (b) Rescaled correlation functions, $C(\Delta x)$ v.s. Δx , where $\Delta x = v\Delta t = r\omega\Delta t$. All rescaled correlation functions collapse to a single curve, indicating a characteristic length scale, Δx_c . Note that the correlation data and power spectrum data from Fig. 6 are related through Wiener-Khinchin Theorem. Inset of (b) shows the correlation function for small t 's, which corresponds to large frequency in the spectra.

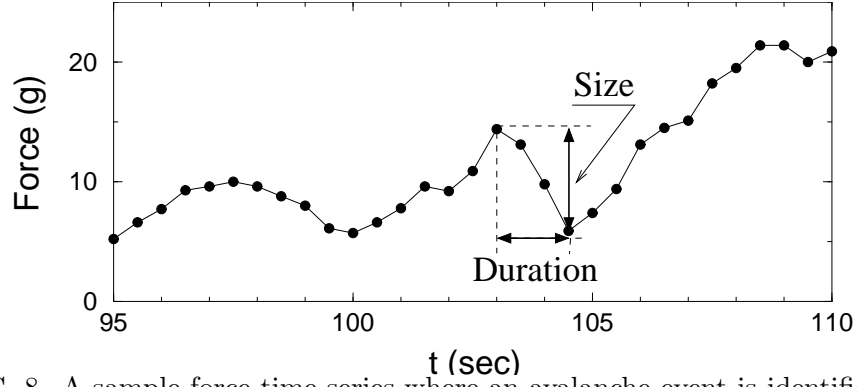


FIG. 8. A sample force time series where an avalanche event is identified.

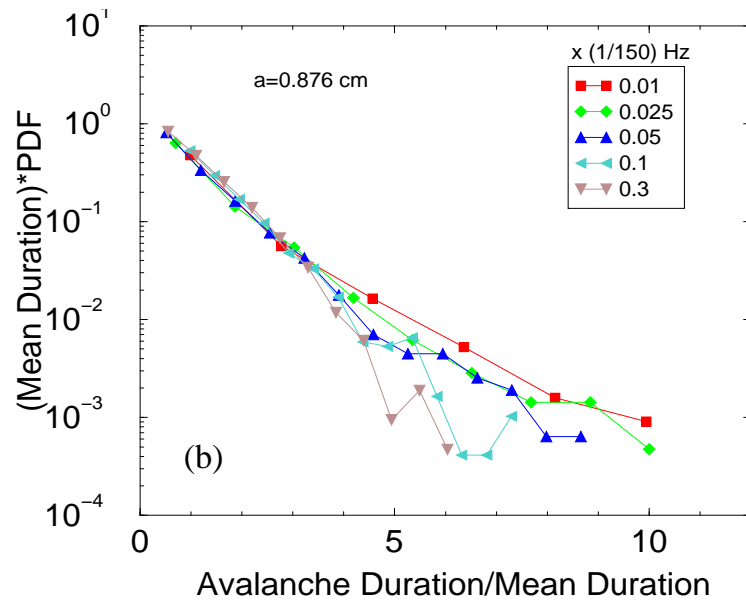
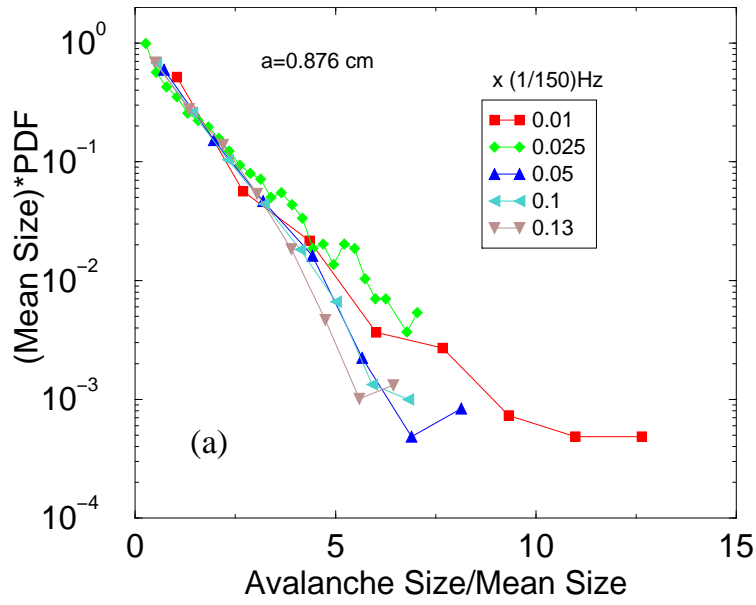


FIG. 9. (a) Rescaled distributions of avalanche size, where the horizontal axis is divided by the mean avalanche size and the vertical axis is multiplied by the mean avalanche size. (b) Rescaled distributions of avalanche duration, where the horizontal axis is divided by the mean avalanche duration and the vertical axis is multiplied by the mean avalanche duration. These distributions indicate an exponential decay of probabilities of finding large avalanche sizes and durations.

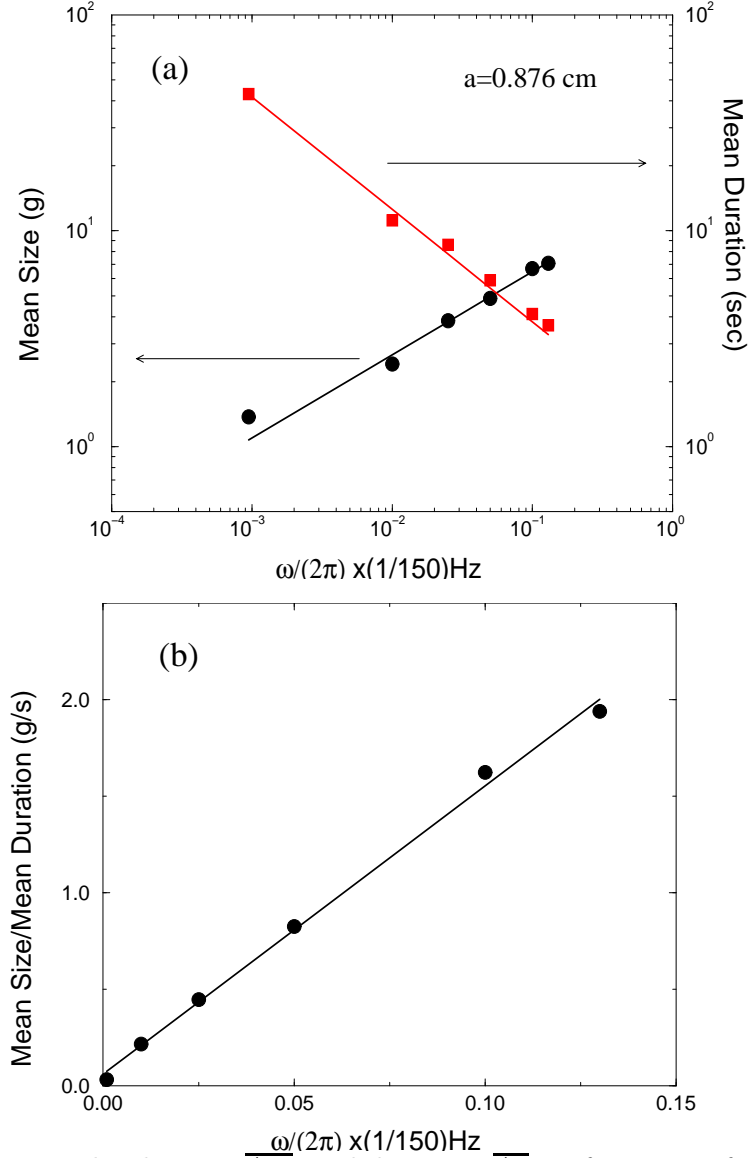


FIG. 10. (a) Mean avalanche size, $\overline{\Delta F}$, and duration, $\overline{\Delta t}$, as functions of the rotation rate, ω . (b) The ratio of the mean avalanche size to duration, $\overline{\Delta F}/\overline{\Delta t}$, as a function of ω .

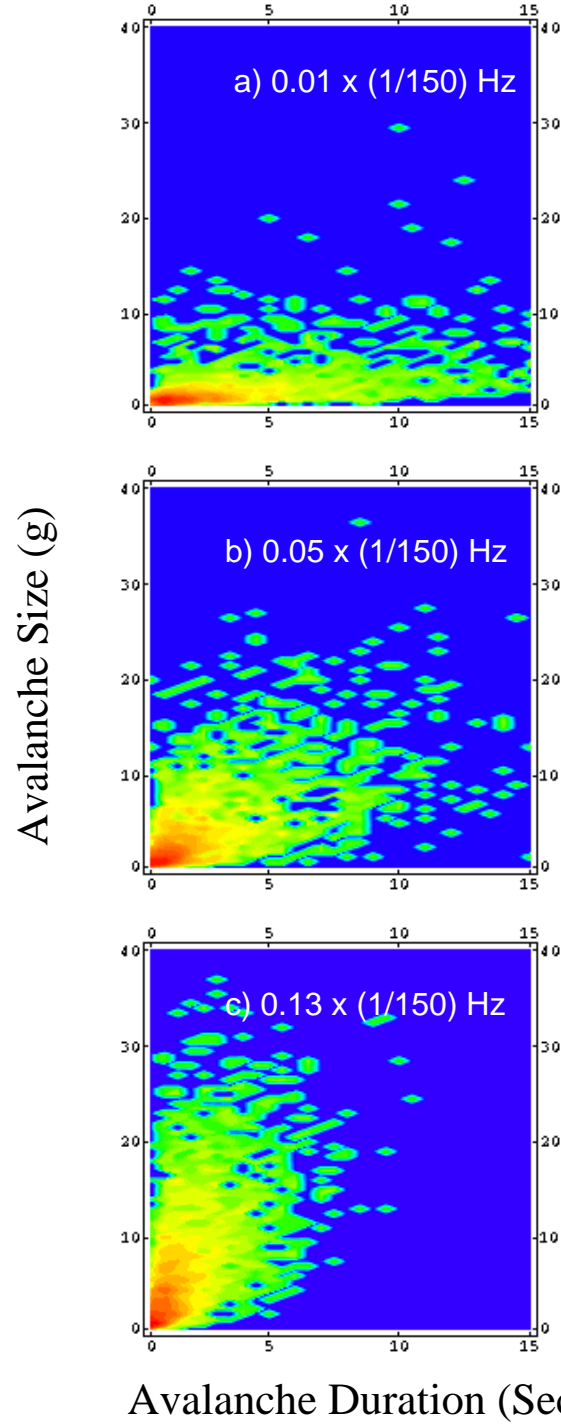


FIG. 11. 2D (greyscale representation) distributions of avalanche size and duration for different rotation rates: (a) $\omega = 0.01 \times (1/150)$ Hz, (b) $\omega = 0.05 \times (1/150)$ Hz, and (c) $\omega = 0.13 \times (1/150)$ Hz. These distributions tend to be largest along certain orientations/slopes. This slope increases when the rotation rate is increased.

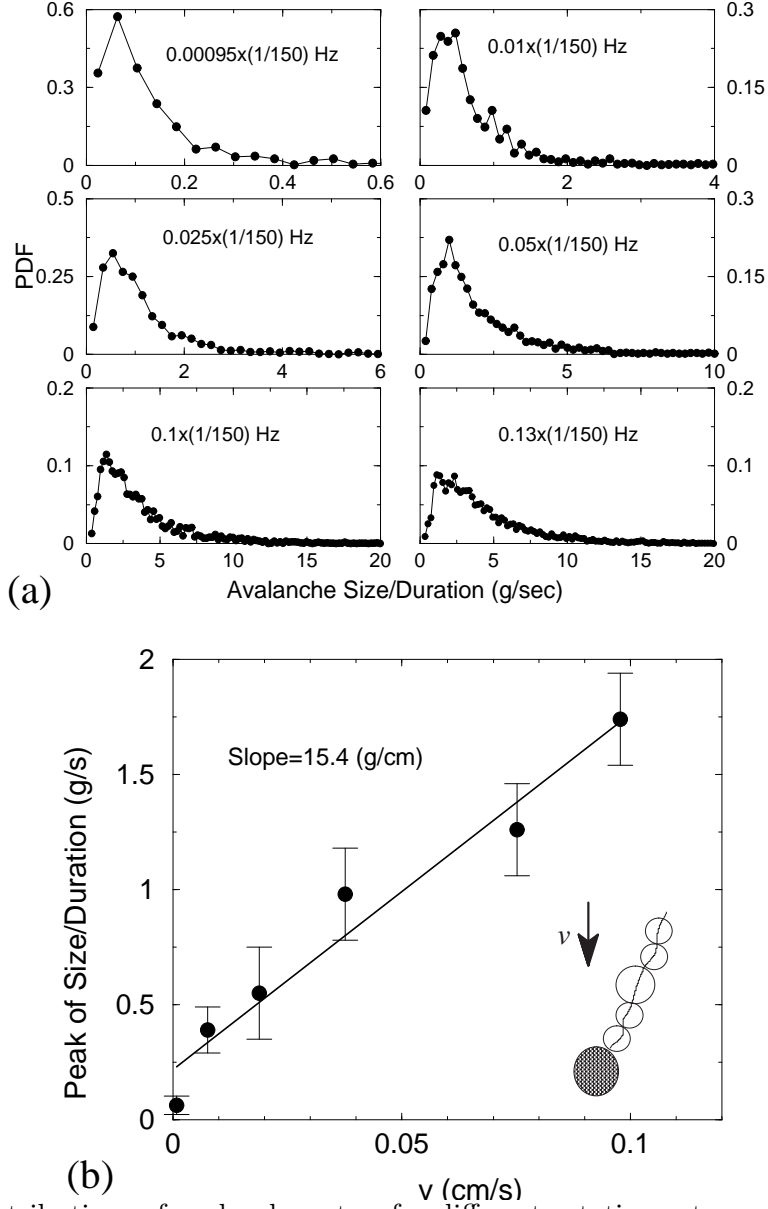


FIG. 12. a) Distributions of avalanche rates, for different rotation rates, where the avalanche rate is defined as the ratio of avalanche size to duration, or roughly the 'slope' of an avalanche. (b) The peaks in the avalanche rate distributions plotted against the rotation speed. The slope of the resulting straight line fit gives an effective force chain force constant, $k_{eff} = \frac{\Delta F}{\Delta t} \frac{1}{v} = \frac{\delta F}{\Delta x}$. The inset shows a schematic of a force chain.

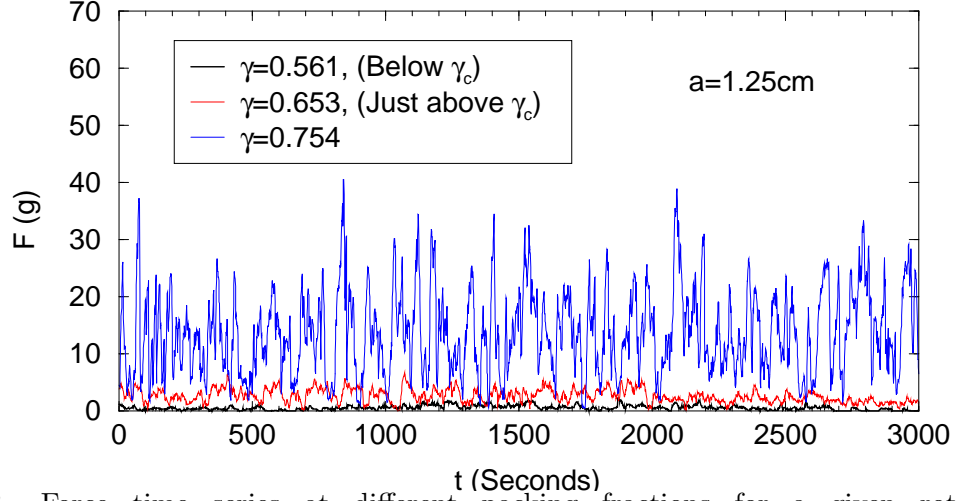


FIG. 13. Force time series at different packing fractions for a given rotation rate ($\omega = 0.075 \times (1/150)$ Hz) and a given tracer size ($a = 1.25$ cm). There exists a critical packing fraction, γ_c , similar to that found in Ref. [8], (see text). Below γ_c , the force is relatively small and the friction between particles and the bottom plate is comparable with the contact force between particles; above γ_c , enduring contact forces dominate and force chains form in the bulk of the system, leading to strong fluctuations in the force time series. The mean drag force increases rapidly when the packing fraction is increased.

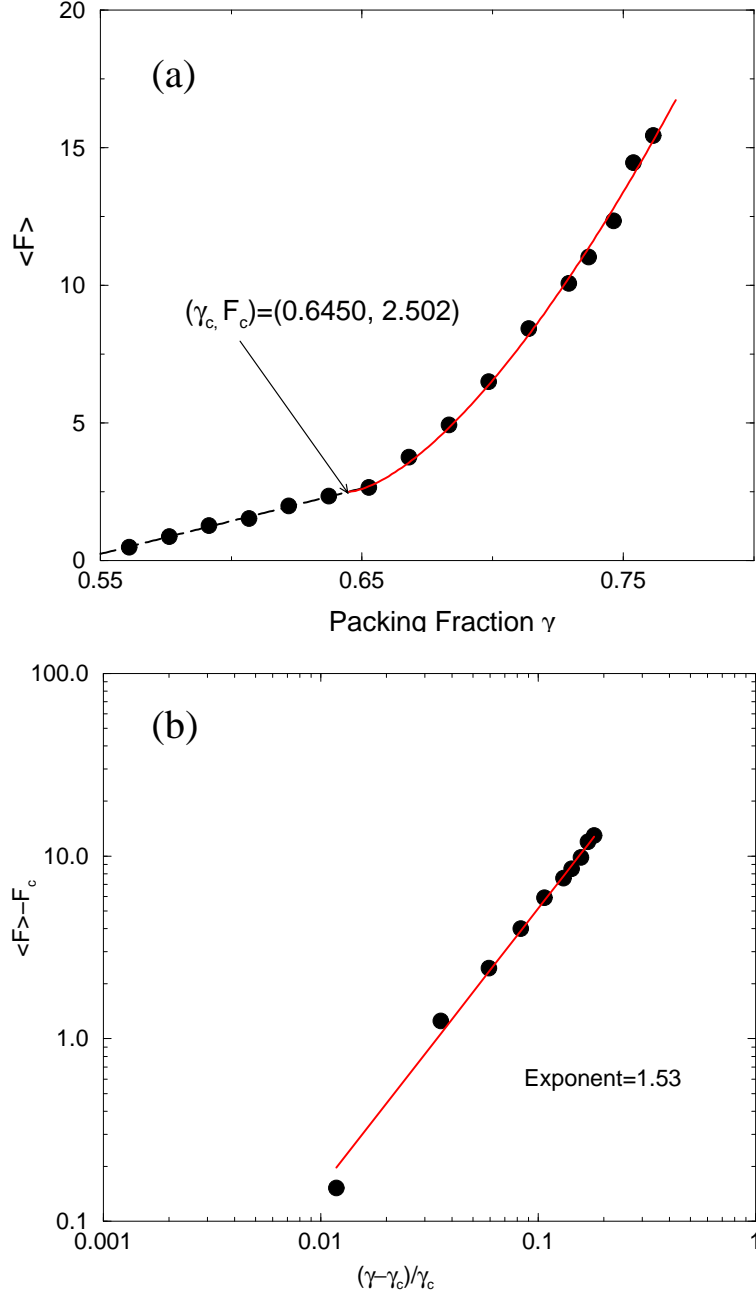


FIG. 14. (a) The mean force, $\langle F \rangle$, as a function of the packing fraction, γ , for a tracer particle of size $a = 1.25$ cm. When γ is below γ_c , the mean force increases linearly with γ ; when γ is above γ_c , the force increases like a power-law, as shown in (b) The mean force as a function of reduced packing fraction, $r = \frac{\gamma - \gamma_c}{\gamma_c}$ for packing fractions greater than γ_c , on log-log scales.

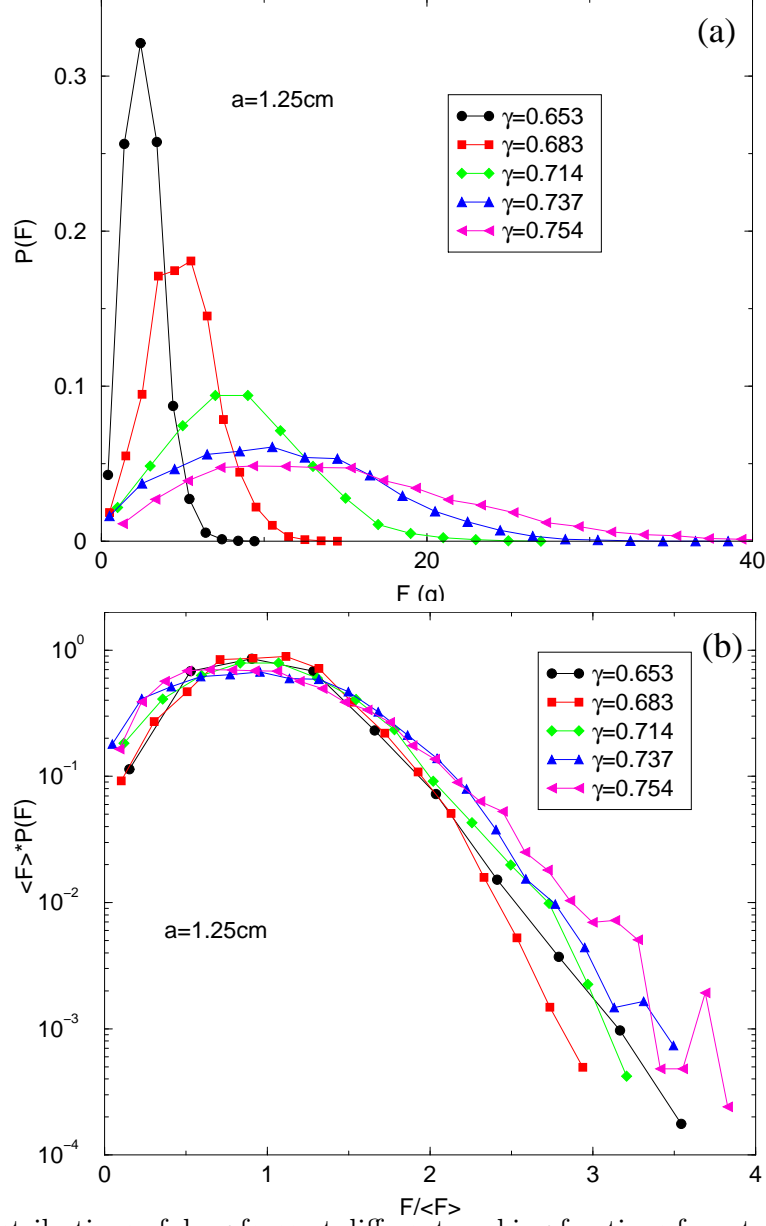


FIG. 15. (a) Distributions of drag force at different packing fractions for a tracer particle of size $a = 1.25$ cm. (b) Same data as (a), but with the horizontal axis rescaled by the corresponding mean force, and the vertical axis multiplied by the mean force. Force distributions collapse reasonably well onto a single curve.

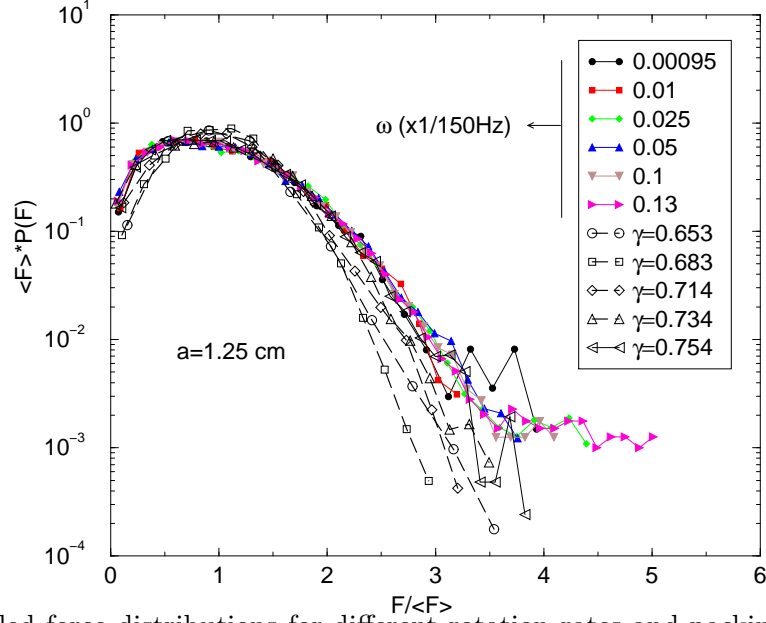


FIG. 16. Rescaled force distributions for different rotation rates and packing fractions. These distributions collapse reasonably well onto a single curve, suggesting a strong statistical invariance after rescaling by the mean force.

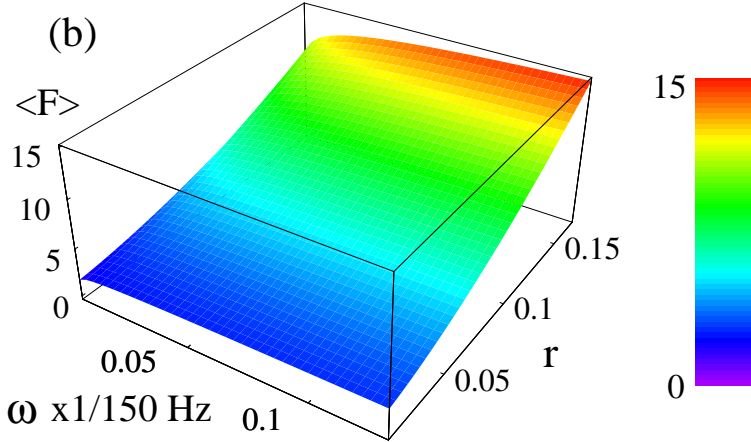
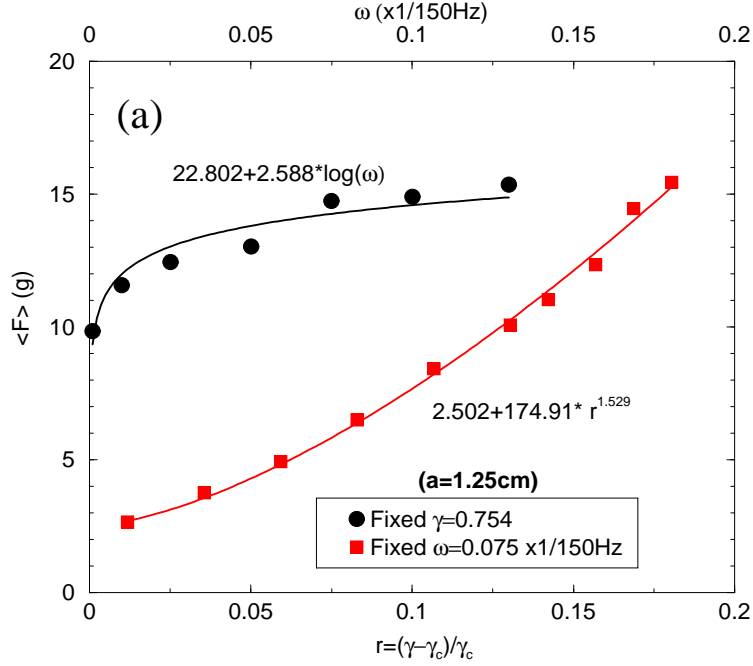


FIG. 17. (a) The mean force as a function of drag velocity and medium packing fraction for a given tracer particle. The solid symbols are experimental data; the lines are a logarithmic fit and a power law fit respectively. (b) With fits obtained from (a), we plot in b) a 3D perspective plot showing how the mean force changes in the parameter space formed by ω and γ . An increase of ω tends to have the same effect on the mean force as an increase of γ , although the former effect is much weaker.

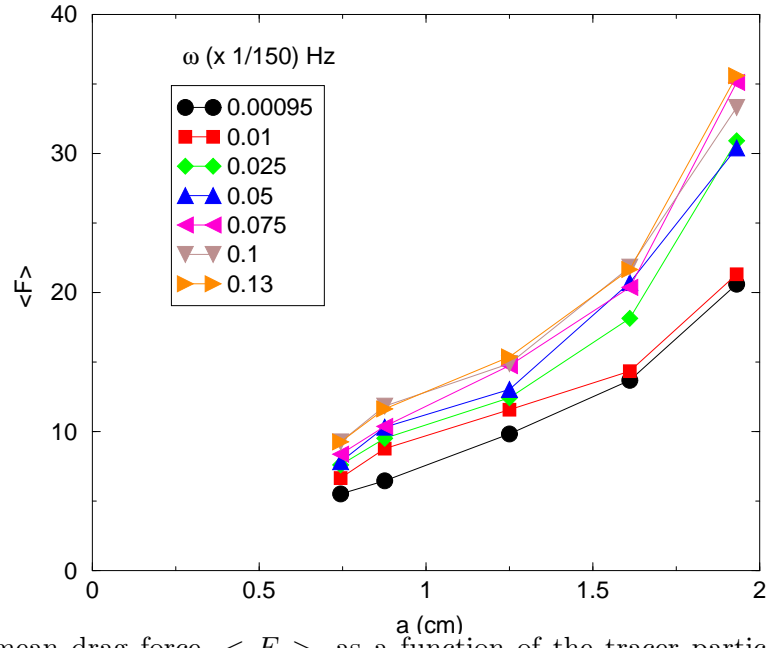


FIG. 18. The mean drag force, $\langle F \rangle$, as a function of the tracer particle diameter, a , for different rotation rates.

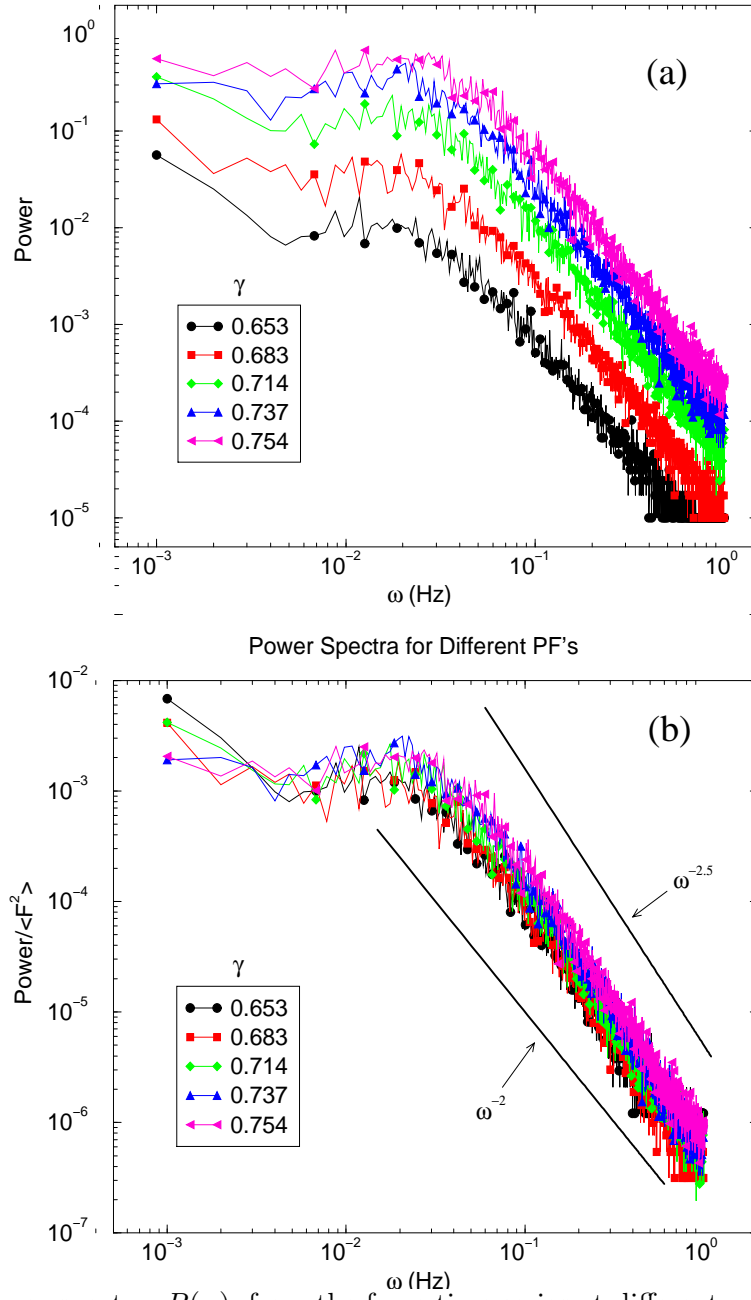


FIG. 19. (a) Power spectra, $P(\omega)$, from the force time series at different packing fractions. (b) Scaled power spectra, with the vertical axis divided by the mean square amplitude of the signal.

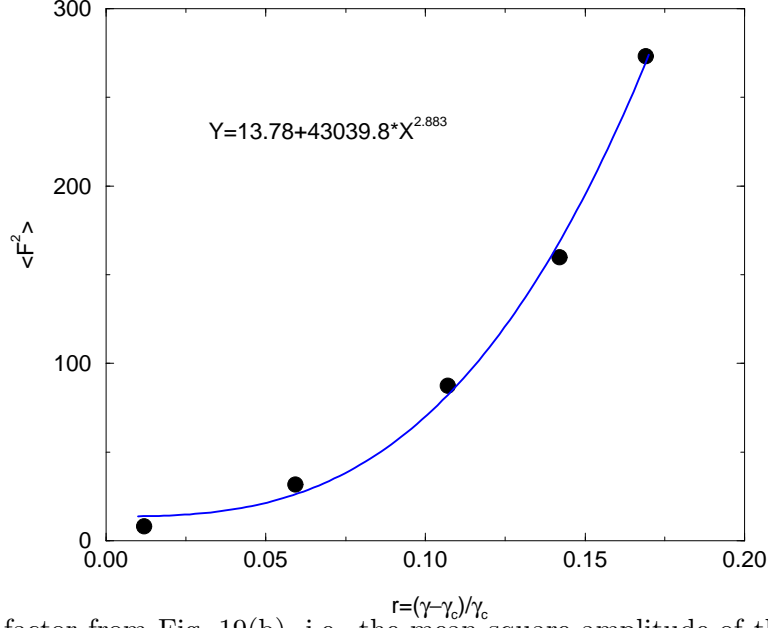


FIG. 20. Scale factor from Fig. 19(b), i.e. the mean square amplitude of the signal, $\langle F^2 \rangle$, vs. reduced packing fraction r . These data again can be fitted by a power law.

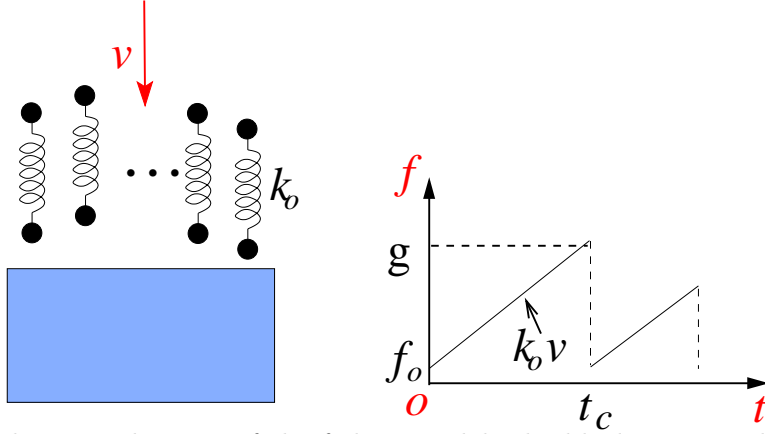


FIG. 21. (a) Schematic drawing of the failure model: the block is a simplified representation of the tracer particle. Force chains in the bulk of the granular system opposing the tracer particle are modeled by springs with a force constant k_0 . The tracer particle is always in balance with the collection of opposing springs/force chains. (b). The force from each spring increases linearly with time, until it fails at the point where the force reaches a threshold value, g . In the physical experiment, this occurs due to the slippage between the tracer particle and the grains, or among grains themselves. After the failure of a spring, the force on the spring is reset, and the threshold is updated with another value drawn from the distribution of thresholds and the process continues.

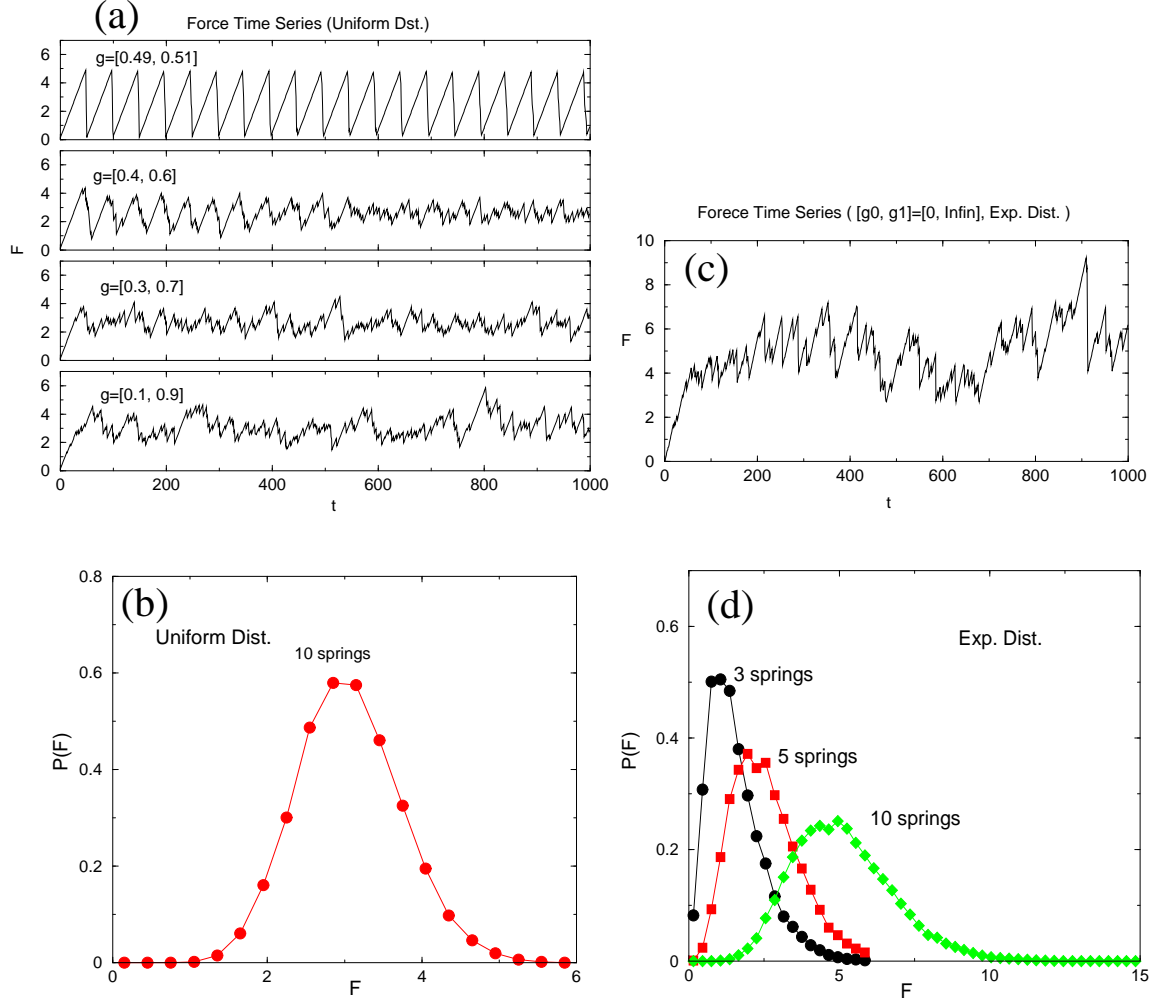


FIG. 22. (a) Force time series generated by the model for various widths of the threshold band, $[g_0, g_1]$, where the threshold is uniformly distributed between the g_0 and g_1 . When the threshold band is narrow, the time series follows a saw-tooth pattern, and when the threshold band is widened, the force time series become more and more random. (b) The force distribution of a random force time series with $[g_0, g_1] = [0.1, 0.9]$, and otherwise as in (a). (c) A random force time series generated from the model with an exponential distribution for the threshold. (d) Force distributions derived from random force time series, such as the one shown in (c), for various numbers of springs. In contrast to (b), the force distribution with an exponentially distributed threshold is non-symmetrical, and more closely resembles the experimental data.

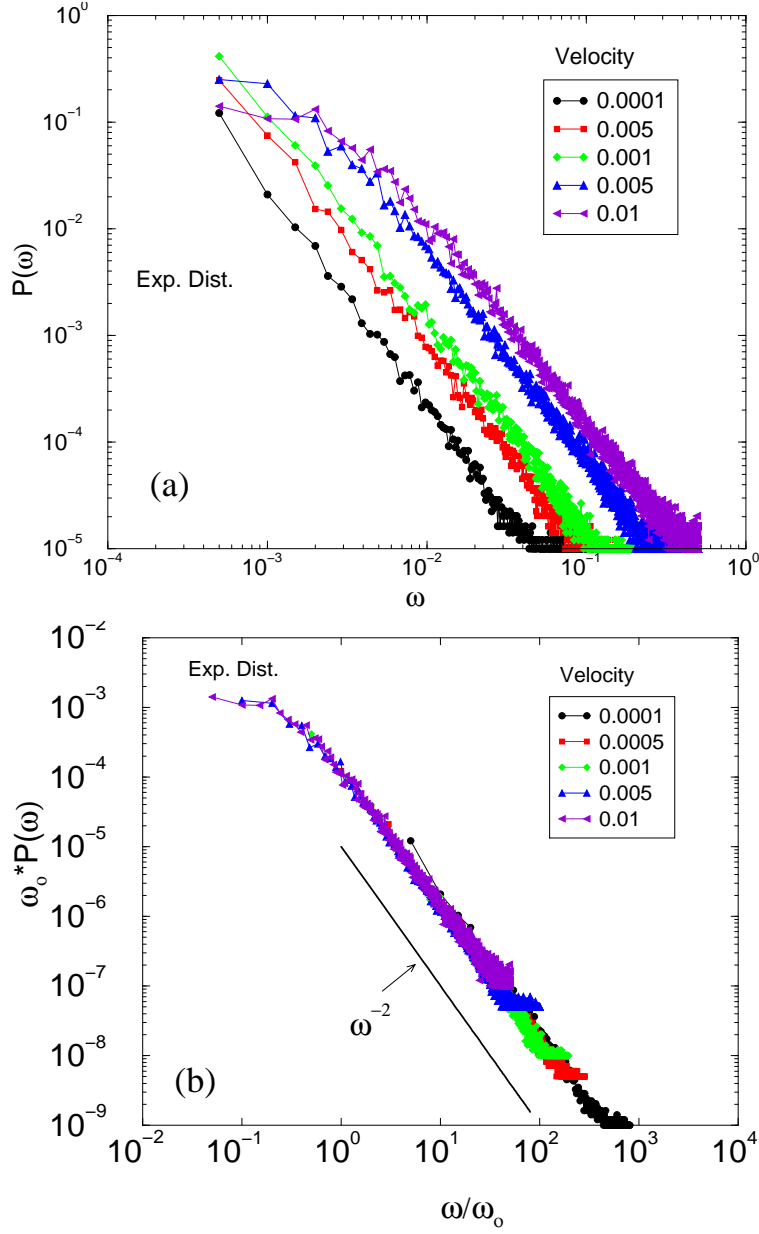


FIG. 23. (a) Power spectra, $P(\omega)$, of the force time series at different rotation rates generated from the model. (b) The scaled power, $\omega_o P(\omega)$ is plotted against the scaled frequency, ω/ω_o , where ω_o is the rotation rate. The rescaled power spectra collapse nicely, and follow a power law decay with an exponent of -2 for higher frequencies, in good agreement with the experimental data shown in Fig. 6.

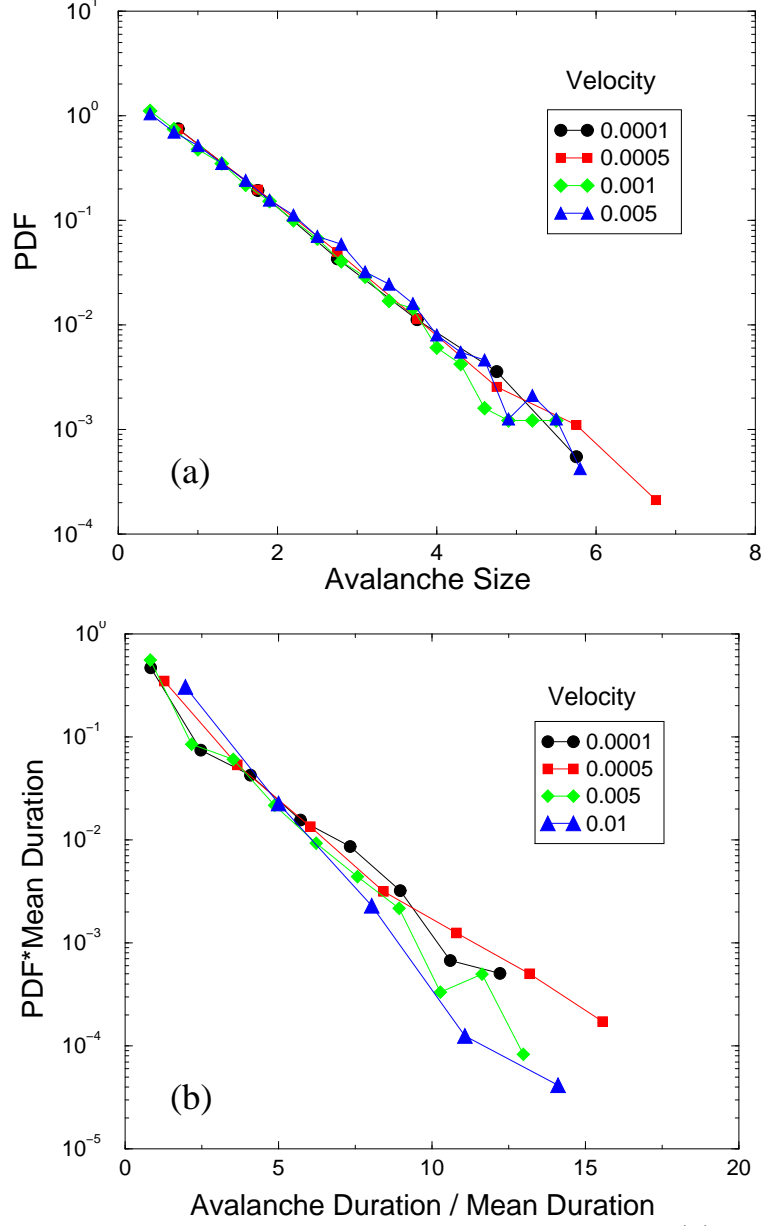


FIG. 24. (a) Distributions of avalanche sizes derived from the model. (b) Rescaled distributions of avalanche durations derived from the model simulations, where the horizontal axis is divided by the mean avalanche duration and the vertical axis is multiplied by the mean avalanche duration. Both distributions of avalanche size and duration are exponential, in agreement with experimental data shown in Fig. 9. However, note that the size distributions in this figure are not scaled while the size distributions in 9a are.

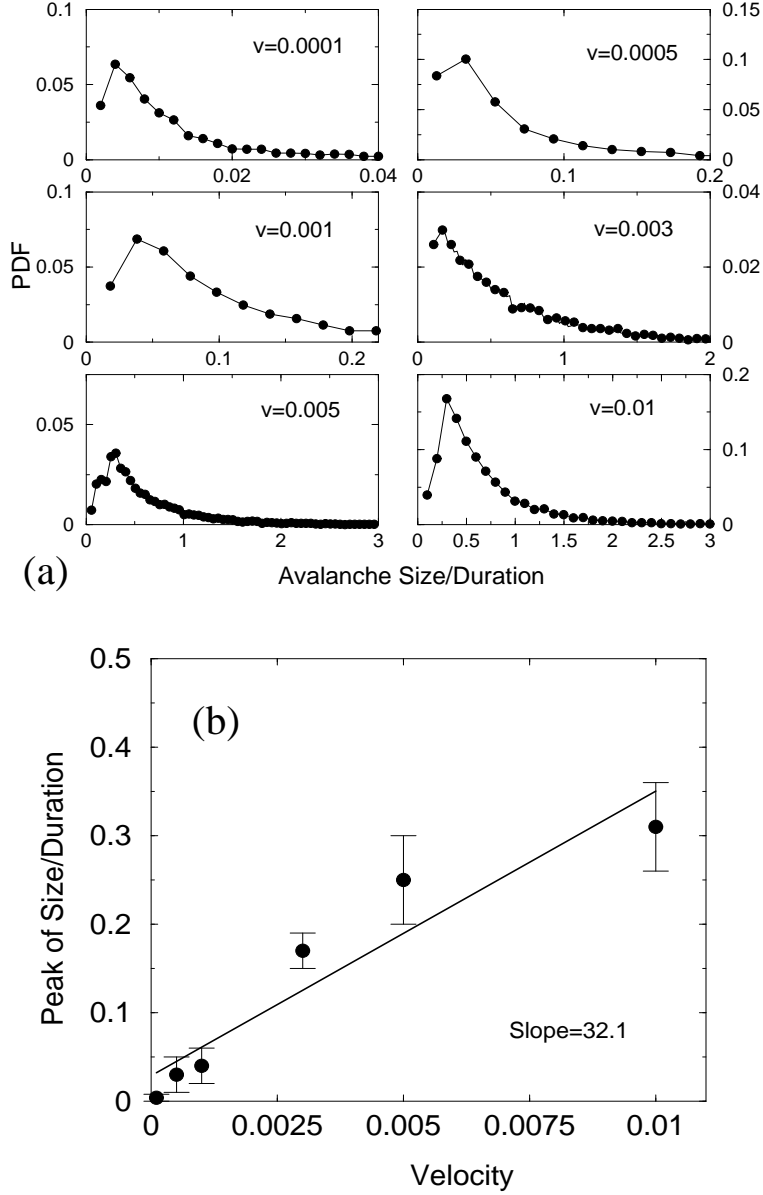


FIG. 25. (a) Distributions of avalanche rates for different rotation rates derived from the model. (b) The force chain force constant, k_{eff} , obtained by fitting a straight line to a plot of the peak of avalanche rate vs. the medium velocity. The value $k_{eff} = 30.7$ is of the same order of magnitude as nk_0 , where $n = 10$ and $k_0 = 1$. This figure compares well with experimental data shown in Fig. 12.

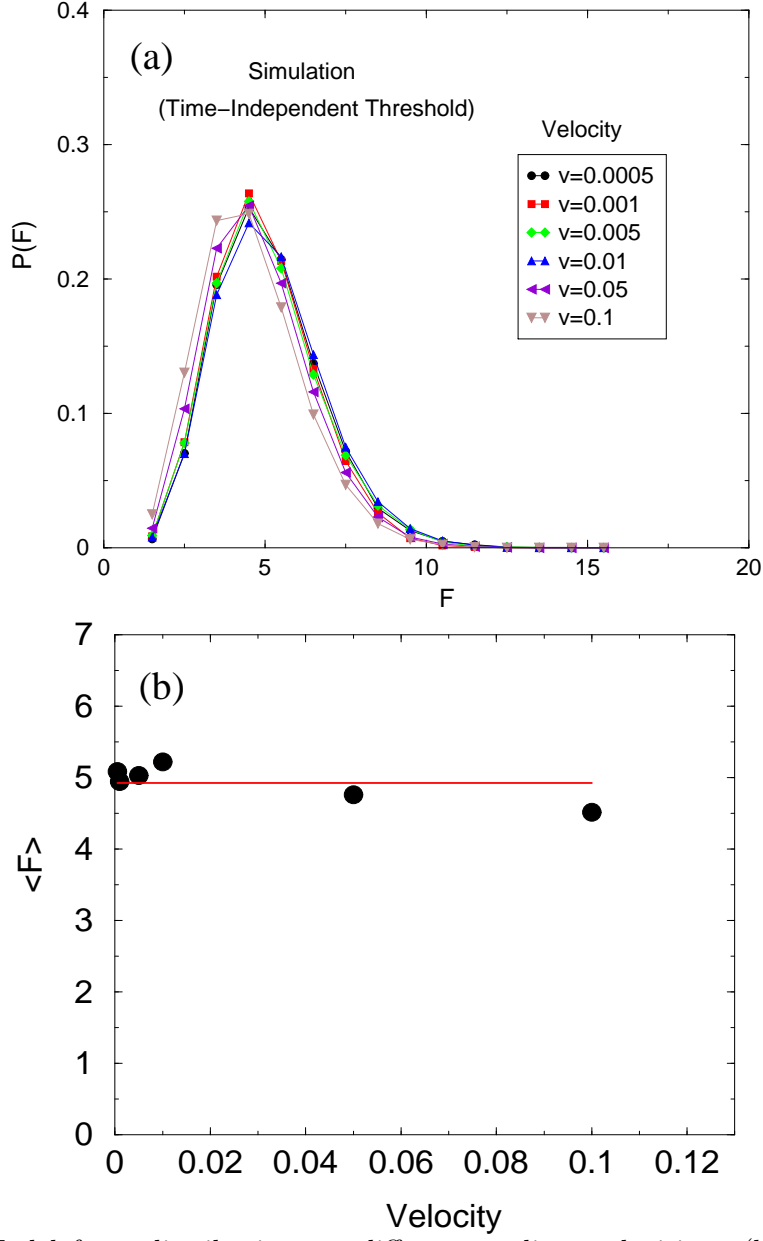


FIG. 26. (a) Model force distributions at different medium velocities. (b) The mean force vs. the medium velocity from model simulations. Both (a) and (b) show that the mean force is independent of the rate. This figure illustrates the problem that the model, so far, cannot account for the experimental finding that the mean force increases slowly with the medium velocity.

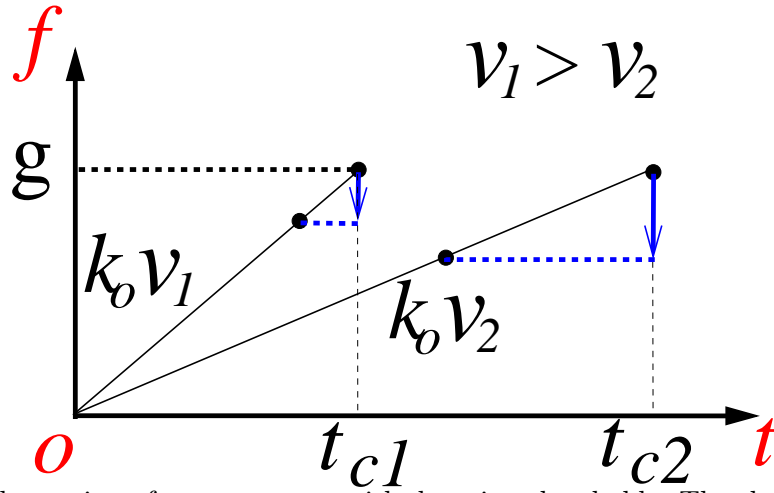


FIG. 27. An illustration of two processes with decaying thresholds. The slower process (v_2 has a waiting time (t_{c2}) and the faster process has a shorter waiting time (t_{c1}). The longer the waiting time, the more the threshold decreases.

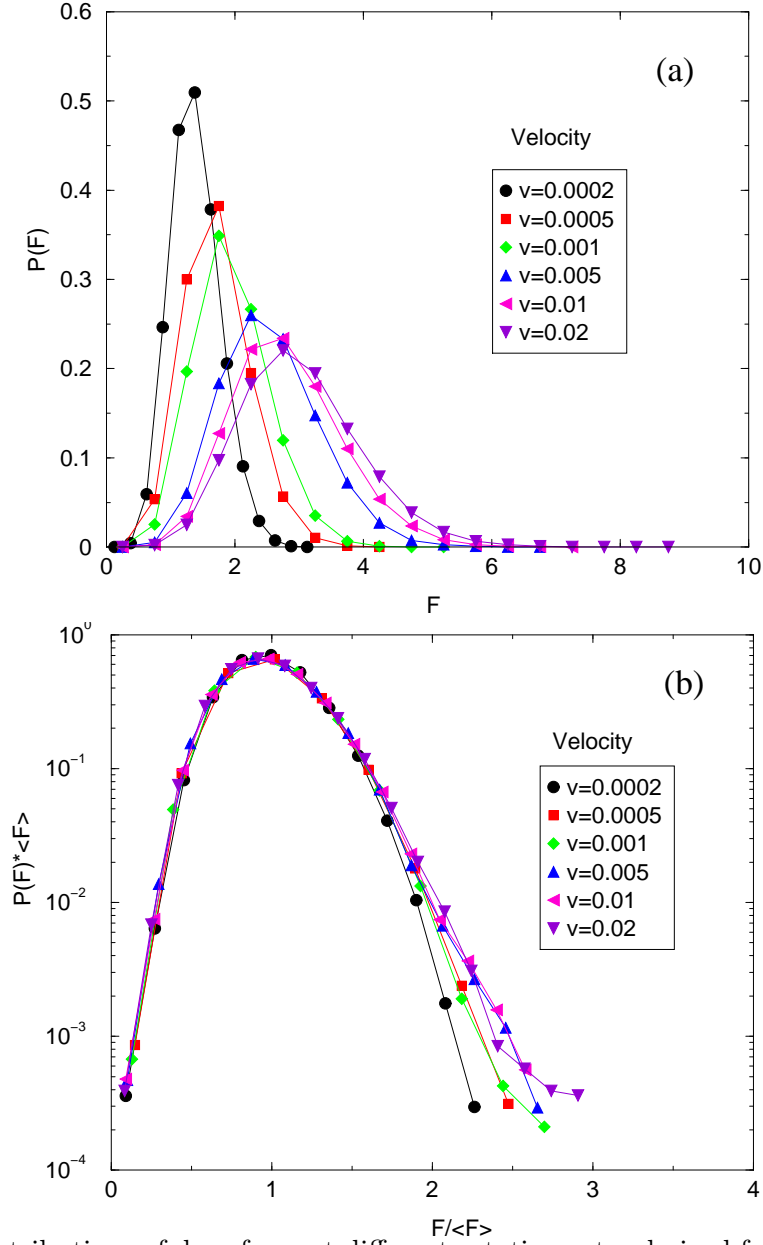


FIG. 28. (a) Distributions of drag force at different rotation rates derived from the simulations when a decaying threshold is used. (b) Same data as (a), but with the horizontal axis rescaled by the corresponding mean force, and the vertical axis multiplied by the mean force. This figure compares well with experimental data shown in Fig. 5.

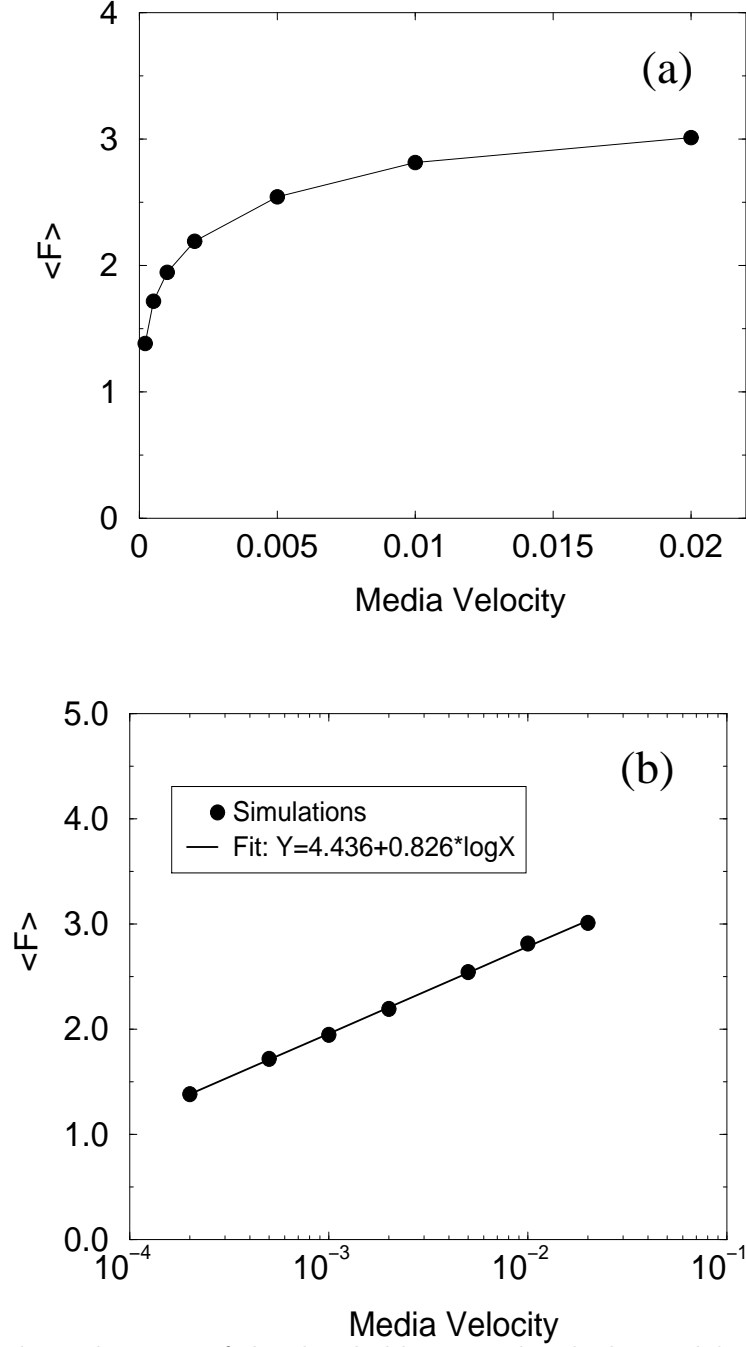


FIG. 29. When slow relaxation of the threshold is considered, the model is able to account for the slow increase of the mean force as the medium velocity is increased. (a) The mean drag force, $\langle F \rangle$, as a function of medium velocity derived from the simulations. (b) Same data as (a), but on a log-lin scale to show the logarithmic increase. This figure compares well with the experimental data of Fig. 3.